

---

---

# FLIGHT DATA ANALYSIS AND FURTHER DEVELOPMENT OF VARIABLE-CONDUCTANCE HEAT PIPES

---

---

## RESEARCH REPORT NO. 2

November 1976

(NASA-CR-137953) FLIGHT DATA ANALYSIS AND  
FURTHER DEVELOPMENT OF VARIABLE-CONDUCTANCE  
HEAT PIPES (TRW Systems Group) 52 p HC  
A04/MF A01

CSSL 20D

N77-14374

Unclas

G3/34 58301

Prepared for  
AMES RESEARCH CENTER  
NATIONAL AERONAUTICS AND SPACE ADMINISTRATION  
Moffett Field, California 94035

**TRW**

FLIGHT DATA ANALYSIS AND FURTHER DEVELOPMENT  
OF VARIABLE-CONDUCTANCE HEAT PIPES  
Research Report No.2

NOVEMBER 1976

Prepared by:  
J. E. Eninger  
D. K. Edwards  
E. E. Luedke

Contract No. NAS 2-8310  
Prepared for:  
Ames Research Center  
National Aeronautics and Space Administration  
Moffett Field, California 94035

**TRW**  
SYSTEMS GROUP

ONE SPACE PARK • REDONDO BEACH, CALIFORNIA

## TABLE OF CONTENTS

		<u>Page</u>
	INTRODUCTION . . . . .	ii
1.0	EXCESS LIQUID IN HEAT-PIPE VAPOR SPACES. . . . .	1
	1.1 FILLETS AND PUDDLES IN VAPOR SPACES . . . . .	2
	1.2 EXCESS LIQUID SLUGGING OF VAPOR SPACES AND THE PRIMING OF ARTERIES . . . . .	12
	1.2.1 Slugging of Open Vapor Spaces. . . . .	12
	1.2.2 Slugging in a Closed Vapor Space . . . . .	15
2.0	THE CAPACITY OF CIRCUMFERENTIAL GROOVES. . . . .	22
3.0	VAPOR FLOW IN HEAT PIPES . . . . .	31
	3.1 THEORETICAL MODEL FOR VAPOR FLOW IN A DEE-SHAPED SPACE	32
	3.1.1 Flow in the Adiabatic Section. . . . .	32
	3.1.2 Flow in Condensing Sections. . . . .	35
	3.1.3 Flow in the Evaporating Section. . . . .	39
	3.2 EXPERIMENTAL VERIFICATION OF THE VAPOR-FLOW MODEL . .	41
4.0	REFERENCES . . . . .	57

## INTRODUCTION

This report is on heat-pipe research carried out for Ames Research Center under contract number NAS 2-8310. The work focuses on the mathematical modeling of three critical mechanisms of heat-pipe operation. In particular, Section 1 is on the effect that excess liquid has on heat-pipe performance; Section 2 is concerned with the calculation of the dryout limit of circumferential grooves; and Section 3 is on an efficient mathematical model for the calculation of the viscous-inertial interaction in the vapor flow. These mathematical models are incorporated in the computer program GRADE II, which is described in Reference (4).

## 1.0 EXCESS LIQUID IN HEAT-PIPE VAPOR SPACES

There are several reasons why heat pipes often operate with more liquid than necessary to just saturate the wick structure. For example, when a heat pipe is designed to operate over a wide temperature range, it is necessary to calculate the fluid charge for the temperature extreme that requires the most fluid. This usually occurs at the lowest operating temperature due to the increase of liquid density with a decrease in temperature; however, it may occur at the highest operating temperature due to the increase of vapor density with an increase in temperature. In either case, for operating temperatures other than the extreme for which the charge just saturates the wick, excess liquid will be present. This source of excess liquid can be particularly significant for gas-loaded variable-conductance heat pipes for use with spacecraft radiators. A relatively high fluid charge is required when the gas blocks a large fraction of the total heat-pipe length and the liquid in the gas-blocked region falls very low in temperature.

Even when the entire heat pipe operates in a narrow temperature range, excess liquid is often intentionally introduced as a safety factor. For some wick types such as axial grooves, a small undercharge can significantly degrade the transport capacity while a small overcharge has little adverse effect. It is particularly important to ensure sufficient liquid in arterial or tunnel-wick heat pipes because even a slight undercharge makes priming impossible.

Excess liquid affects heat-pipe performance in various ways. It resides in the heat-pipe vapor spaces and forms liquid fillets along corners and a puddle along the bottom. These fillets and puddles provide low-permeability flow paths in parallel with the wick structure. Their size at a given axial location depends on the local value of the vapor-liquid pressure difference, or capillary stress. Thus, excess liquid usually has the greatest effect in the condenser region where the stress is low.

In addition to contributing to the axial transport of liquid, a puddle reduces the hydrostatic stress that the wick must support. Although excess liquid increases axial-transport capacity, it degrades the heat transfer, because fillets and puddles block condensation surface. The condenser end

of a vapor space can even completely fill a liquid slug that blocks condensation heat transfer in that region altogether. An accurate mathematical model of excess-liquid behavior is particularly needed for the graded-porosity-wick heat pipe, where to maximize its capacity the wick is begun at the condenser end with the highest possible porosity. If the porosity is too high, however, the wick will not generate a sufficient capillary pressure to prevent a liquid slug from forming.

The mathematical modeling of excess liquid is complicated by the fact that for typical heat pipes one cannot neglect variations of hydrostatic pressure with position on the free surface of the liquid. An earlier mathematical model in the heat-pipe computer program MULTIWICK<sup>(1)</sup> neglected these variations. Although the resulting simplification allowed application quite general heat-pipe cross-sectional geometries, at low values of capillary stress the results are only qualitatively correct. To retain the hydrostatic pressure variations in the present work, it is necessary to select specific types of cross-sectional geometries for the vapor spaces. We have selected the circular vapor space which occurs in axially-grooved heat pipes and simple heat pipes with wick-lined wall, and "Dee-shaped" vapor spaces formed by slab wicks in circumferentially grooved tubes. Section 1.1 presents methods for calculating the contribution of excess liquid to axial transport, and Section 2.2 presents both theoretical and experimental results for conditions under which liquid slugs form in the vapor spaces. These results also apply to arteries, so we digress in Section 1.2 to discuss criterion for the priming of open-and-closed arteries.

## 1.1 FILLETS AND PUDDLES IN VAPOR SPACES

The three geometries considered are shown in Figure 1-1, where typical fillets and puddles are drawn as they might appear at a specific axial location of a heat pipe operating in earth gravity. The key parameter that governs the configuration of the excess liquid is vapor-liquid pressure difference. Since it varies hydrostatically transverse to the heat pipe, in order to have a unique value at every axial location, we take its value along the centerline of the heat pipe and define it as the capillary stress.

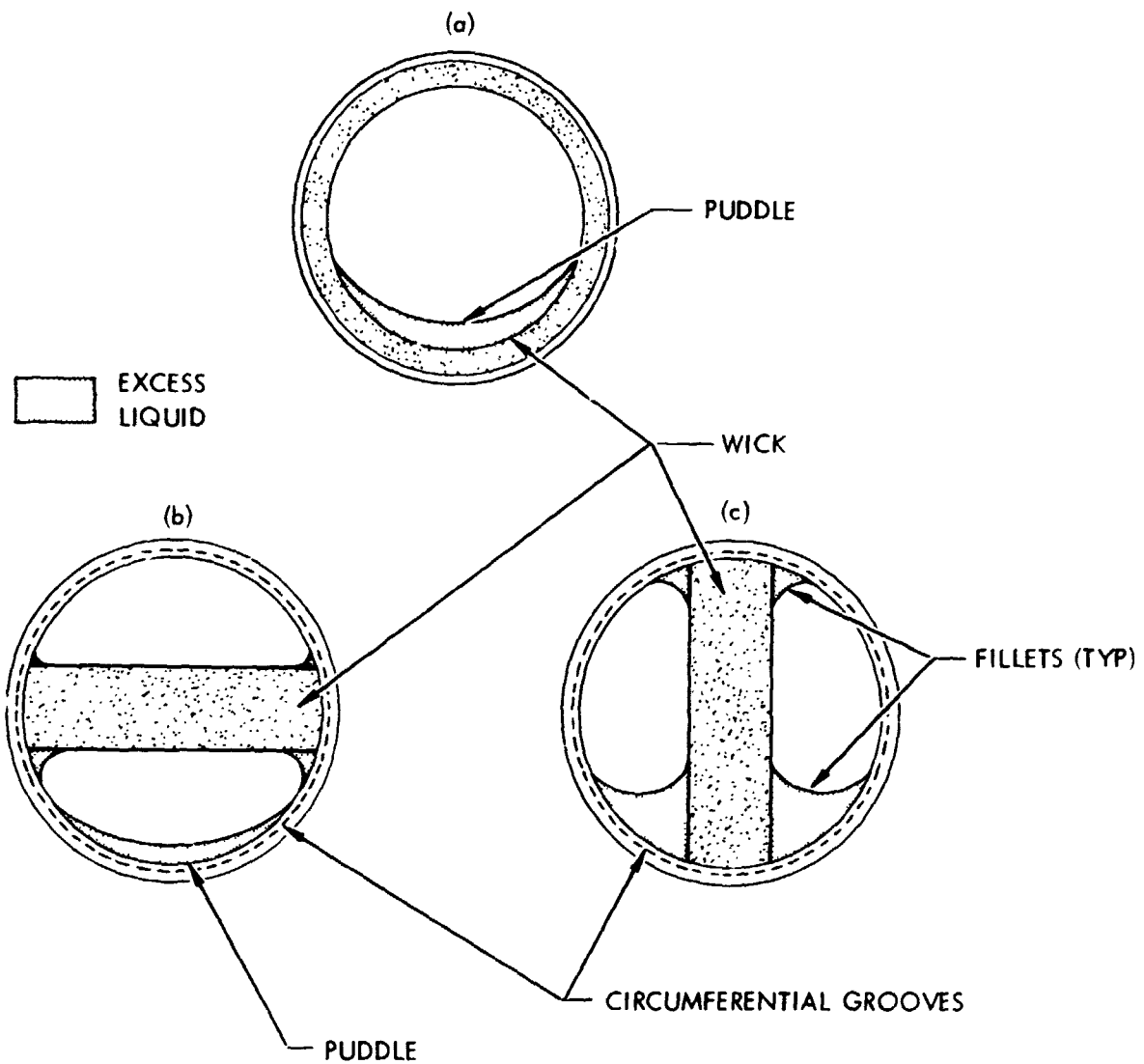


Figure 1-1. The three geometries considered for the excess - liquid model - (a) circular vapor space, (b) horizontal slab wick, (c) vertical slab wick.

As the stress decreases, the size of the fillets and puddles increases. If the stress is sufficiently low, the vapor space will bridge and a liquid slug will form, which is the subject of the next section. We now present methods for the calculation of the free-surface shape of a fillet or puddle, its cross-sectional area, and its free and wetted perimeter.

The equation governing the free surface of a liquid under the action of surface tension is

$$\Delta P = \sigma(1/R_1 + 1/R_2), \quad (1.1)$$

where  $\Delta P$  is the local pressure difference between the gas and liquid,  $\sigma$  is the surface tension, and  $R_1$  and  $R_2$  are the local radii of curvature in any two orthogonal planes that contain the normal to the surface. As the first of these, we take the x-y plane of the heat-pipe cross section. By assuming that the cross-sectional shape of the fillet or puddle changes gradually with distance along the heat pipe, we can neglect the reciprocal of the second radius of curvature compared to that of the first, and Eq. (1.1) reduces to

$$\Delta P = \sigma/R \quad (1.2)$$

A differential equation is obtained for the free-surface shape by substituting for  $\Delta P$  the hydrostatic pressure variation with y and by substituting for R the Cartesian formula for the radius of curvature, which results in

$$\rho g y = \frac{d^2 y / dx^2}{[1 + (dy/dx)^2]^{3/2}} \quad (1.3)$$

Here  $\rho$  is the difference in the liquid and vapor densities, and g is the gravitational acceleration. Also, the location of the coordinates is chosen such that the gas-liquid pressure difference is zero when y = 0. Equation (1.3), however, presents difficulties because one cannot integrate readily through regions where dy/dx is infinite. To remedy this, we use the transformation

$$dy/dx = \tan \alpha \quad (1.4)$$

to transform Eq. (1.3) into two differential equations where the dependent variables are x and y and the independent variable is the inclination  $\alpha$  of



the free-surface curve. The resulting equations are

$$2y \, dx/d\alpha = a^2 \cos \alpha, \quad (1.5)$$

$$2y \, dy/d\alpha = a^2 \sin \alpha, \quad (1.6)$$

$$\text{where } a = \sqrt{2\sigma/\rho} \quad (1.7)$$

is the capillary constant. Equation (1.6) is readily integrated, which results in

$$y = \sqrt{y_0^2 - a^2 (\cos \alpha - \cos \alpha_0)} \quad (1.8)$$

where the curve has an inclination  $\alpha_0$  at a point  $(x_0, y_0)$ . With the solution (1.8), we can eliminate  $y$  from Eq. (1.5), which gives

$$dx/d\alpha = \frac{a^2 \cos \alpha}{2 \sqrt{y_0^2 - a^2 (\cos \alpha - \cos \alpha_0)}} \quad (1.9)$$

This equation can be integrated in terms of elliptic integrals by first using the transformation  $\alpha = 2\phi - \pi$ , which allows us to rewrite Eq. (1.9) as

$$dx = \frac{\sqrt{2}}{2} a \, k \left[ \frac{2 \sin^2 \phi - 1}{\sqrt{1 - k^2 \sin^2 \phi}} \right] d\phi, \quad (1.10)$$

where

$$k = \frac{2a^2}{a^2(1 + \cos \alpha_0) + y_0^2} \quad (1.11)$$

One can easily verify that the solution to Eq. (1.10) in terms of elliptic integrals of the first kind  $F(k, \phi)$  and of the second kind  $E(k, \phi)$  is

$$x = \left( \frac{\sqrt{2}}{k} a \right) \{ (1 - k^2/2) [F(\phi, k) - F(\phi_0, k)] - [E(\phi, k) - E(\phi_0, k)] \} + x_0 \quad (1.12)$$

where  $\phi_0$  is the value of  $\phi$  when  $\alpha = \alpha_0$ .

Equations (1.8) and (1.12) define a single free-surface curve that passes through the point  $(x_0, y_0)$  at an inclination  $\alpha_0$ . The task now is to fit a segment of that curve inside the cross-sectional geometry of the heat pipe such that it represents a fillet or puddle. As seen in Figure 1-1, in the case of a fillet the boundary conditions require that, for a zero wetting angle, one end of the segment is tangent to the slab wick and the other is

tangent to the tube wall. We will describe how the solution is found for the puddle and for one particular fillet. The method for the other fillets is the same except for the details.

Consider first, as shown in Figure 1-2, the solution for the puddle. The point at the bottom of the puddle is taken as the point  $(x_0, y_0)$ , where  $x_0 = 0$ ,  $\alpha_0 = 0$ , and  $y_0$ , which sets the gas-liquid pressure difference at the surface of the puddle, is a selected positive value. Points  $(x, y)$  along the free-surface curve which are calculated from Eqs. (1.8) and (1.12) for increasing values of  $\alpha$ , are checked to see if the condition of tangency with the tube wall is met, which is

$$x - R_T \sin \alpha = 0 \quad (1.13)$$

Figure 1-2(b) shows that there is a second tangency condition for which Eq. (1.13) is satisfied. Thus the same free-surface curve can represent two puddles.

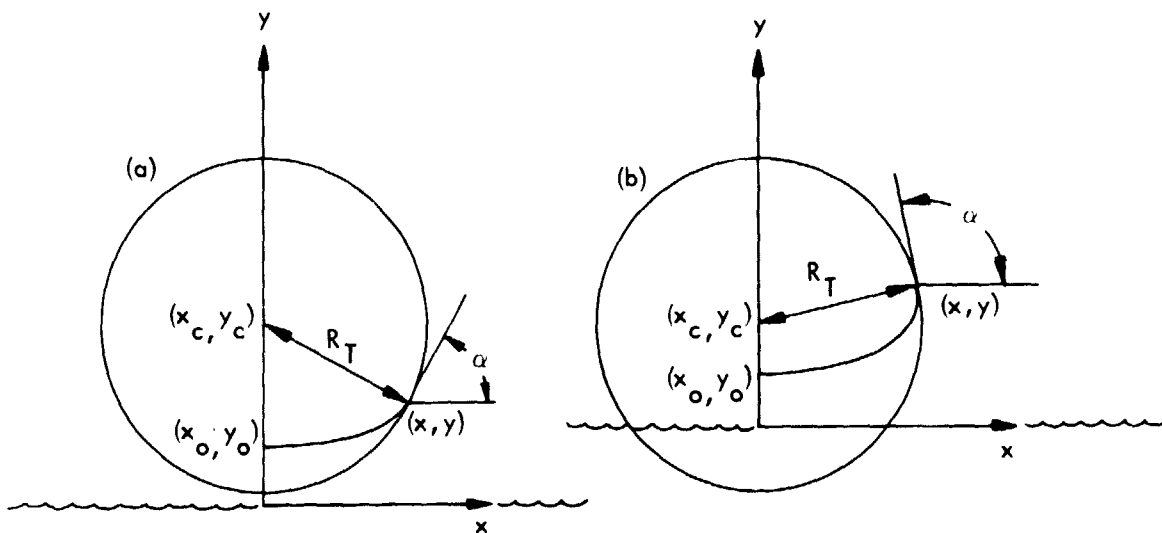


Figure 1-2. Tangency Condition:  $x = R_T \sin \alpha$   
 (a)  $\alpha < \pi/2$       (b)  $\alpha > \pi/2$

The capillary stress (gas-liquid pressure difference at the center of the tube) is given by

$$\rho g y_c = \rho g(y + R_T \cos \alpha) \quad (1.14)$$

where  $y$  and  $\alpha$  are the values at the point of tangency. A series of puddles are calculated for different values of capillary stress by starting with different values for  $y_0$ .

The bottom fillet that forms in a heat pipe with a vertical slab wick [Figure 1-1 (c)] is calculated exactly the same as a puddle with Eqs. (1.13) and (1.14) applying except that the initial condition is  $x_0 = T/2$  and  $\alpha_0 = -\alpha/2$ . Again two fillets are possible from a given free-surface curve. The other types of fillets depicted in Figure 1-1 are calculated by a similar method except for these only a single fillet is possible for a given free-surface curve.

We now turn to the calculation of areas, wetted perimeter and free perimeter. Although the free perimeter is not used in the calculation of the effective permeability of the excess liquid, it is an important parameter for future work on vapor-liquid interaction. An elemental length  $dS_f$  of the free perimeter  $S_f$  is given by

$$dS_f = \sqrt{dx^2 + dy^2} \quad (1.15)$$

With the use of Eqs. (1.5), (1.6) and (1.8), we rewrite Eq. (1.15) as

$$dS_f = \frac{a^2 d\alpha}{2\sqrt{y_0^2 - a^2(\cos \alpha - \cos \alpha_0)}} \quad (1.16)$$

As in the solution of Eq. (1.9), we use the transformation  $\alpha = 2\phi - \pi$  to write  $dS_f$  as

$$dS_f = \sqrt{2} ka \frac{d\phi}{\sqrt{1 - k^2 \sin^2 \phi}} \quad (1.17)$$

where  $k$  is given by Eq. (1.10). Equation (1.16) integrates to

$$S_f = \sqrt{2} ka [F(\phi, k) - F(\phi_0, k)] \quad (1.18)$$

For the calculation of the area, refer to Figure 1-3 (a). Although a particular fillet is shown, the expressions derived below apply directly to the puddle and other fillets as well. The area desired is  $A_f = A_{0a2b3}$ , where the subscripts denote points and lines bounding the area. It is more convenient, however, to calculate  $A_{0a2}$ . Then, the desired area is

$$A_f = A_{023} + (A_{12b3} - A_{123}) - A_{0a2} \quad (1.19)$$

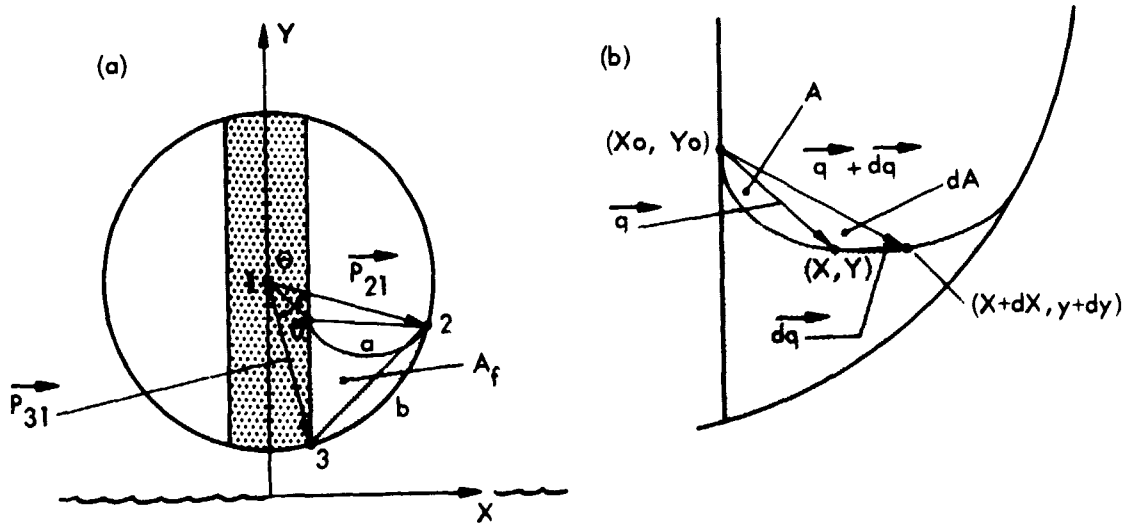


Figure 1-3. Calculation of the fillet area  $A_f$ .

(a) Diagram defining points, lines and vectors.

(b) A blow-up of Figure 1-3 (a) showing the vector  $q$  that connects  $(x_0, y_0)$  to a point  $(x, y)$  on the free-surface curve.

The area of triangles  $A_{023}$  and  $A_{123}$  are calculated in terms of the coordinates for their vertices:

$$A_{123} = \frac{1}{2} |(x_2 y_3 - y_2 x_3) - (x_1 y_3 - y_1 x_3) + (x_1 y_2 - y_1 x_2)| \quad (1.20)$$

$$A_{023} = \frac{1}{2} |(x_2 y_3 - y_2 x_3) - (x_0 y_3 - y_0 x_3) + (x_0 y_2 - y_0 x_2)| \quad (1.21)$$

The area of the sector  $A_{12b3}$  is  $1/2 \theta R_T^2$ , where  $\theta$  is the angle between vectors  $\vec{P}_{21}$  and  $\vec{P}_{31}$ :

$$\begin{aligned}\theta &= \cos^{-1} \frac{\vec{P}_{31} \cdot \vec{P}_{21}}{|\vec{P}_{31}| |\vec{P}_{21}|} \\ &= \frac{(x_3 - x_1)(x_2 - x_1) + (y_3 - y_1)(y_2 - y_1)}{\sqrt{[(x_3 - x_1)^2 + (y_3 - y_1)^2][(x_2 - x_1)^2 + (y_2 - y_1)^2]}} \quad (1.22)\end{aligned}$$

It remains to calculate  $A_{oa2}$ . Consider Figure 1-3 (b) where the vector  $\vec{q}$  connects the point  $(x_0, y_0)$  to a general point along the free-surface curve. The area between  $\vec{q}$  and the curve is  $A$ . We now calculate the increase in area  $dA$  when  $\vec{q}$  is incremented an amount corresponding to the increment  $d\alpha$ . The incremental area  $dA$  is the area of the triangle bounded by  $\vec{q}$  and  $d\vec{q}$ , thus

$$dA = \frac{1}{2} |\vec{q} \times d\vec{q}| \quad (1.23)$$

With  $\vec{q} = (x - x_0) \vec{i} + (y - y_0) \vec{j}$  and  $d\vec{q} = dx \vec{i} + dy \vec{j}$ , we find

$$dA = \frac{1}{2} |dy(x - x_0) - dx(y - y_0)| \quad (1.24)$$

Equations (1.5) and (1.6) are used to obtain

$$\frac{dA}{d\alpha} = \frac{a^3}{4y} |(x - x_0) \sin \alpha - (y - y_0) \cos \alpha| \quad (1.25)$$

Since  $x$  is given in terms of elliptic integrals, there is no hope of obtaining an analytic integral for  $A$ . Therefore, the integration is carried out numerically from  $\alpha_0$  to the point where the boundary condition on the tube wall is met.

Referring to Figure 1-3 (a), we see that the wetted perimeter is given simply by  $S_w = y_0 - y_3 + R_T \theta$ . (1.26)

The computer FILLET<sup>(2)</sup> was written to carry out the calculations outlined in this section. Since we could not find a general-purpose subroutine for elliptic integrals, Eqs. (1.9) for  $x$  and (1.17) for  $S_f$  are

integrated numerically along with Eq. (1.24) for A. The output from FILLET is a table of effective hydraulic diameter and the total area of fillets and a puddle for the range of capillary stress that can exist in a heat pipe.

To illustrate the calculations, we focus attention on the puddle in a circular vapor space. Two parameters are required to fix the puddle configuration. The first is the Bond number

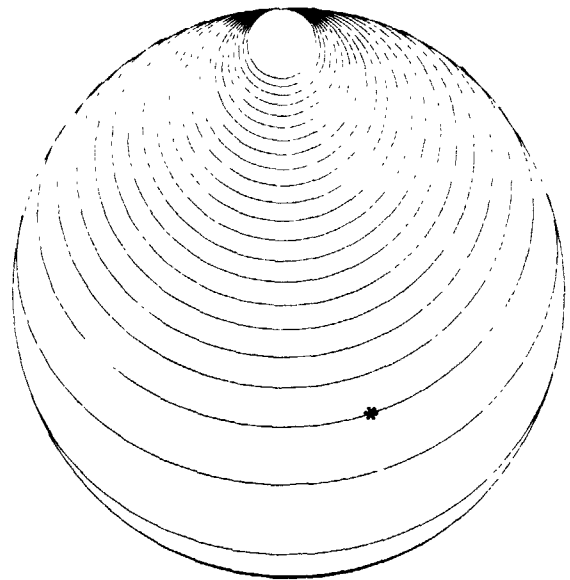
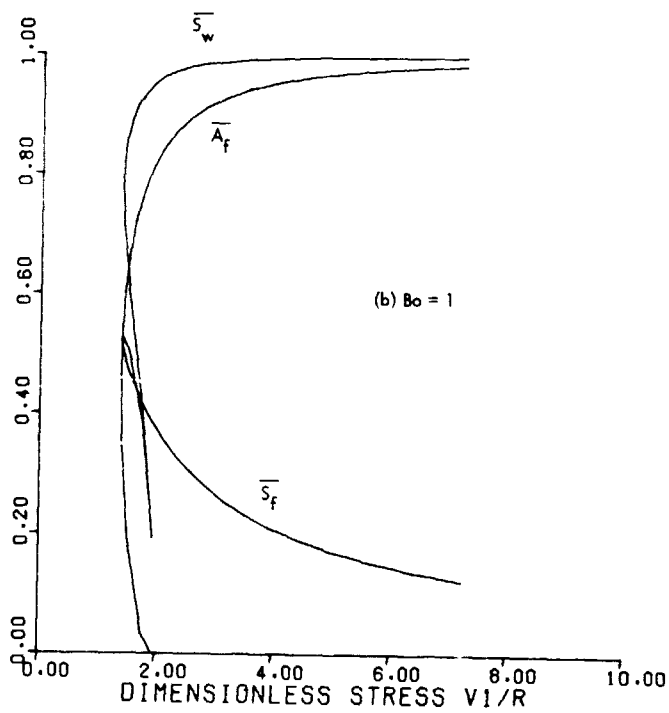
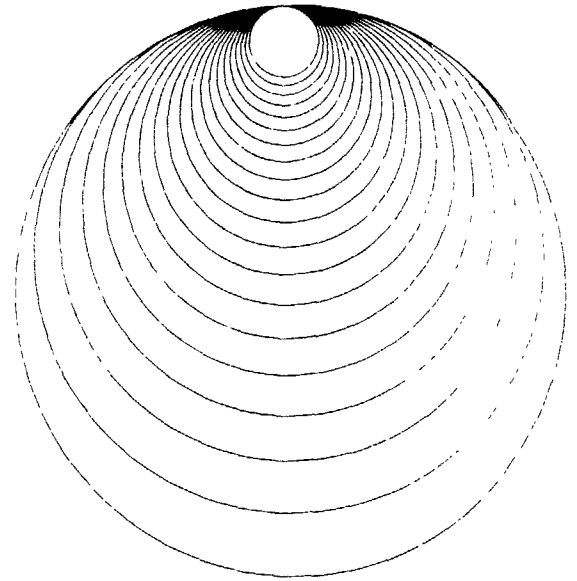
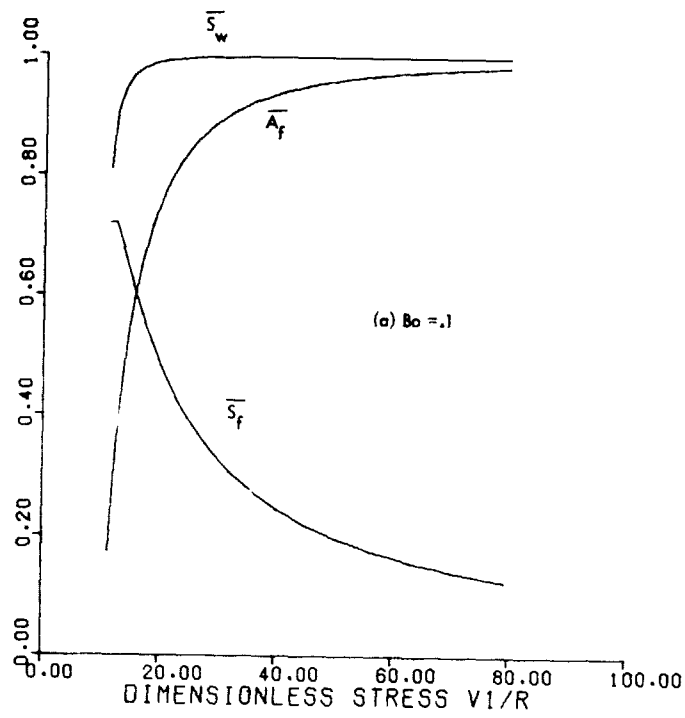
$$B = \rho g R_T^2 / \sigma, \quad (1.27)$$

which is the ratio of hydrostatic forces to surface tension. The second parameter is the dimensionless capillary stress

$$S = P_0 / \rho g R_T, \quad (1.28)$$

where  $P_0$  is the gas-liquid pressure difference at the center of the tube. For a geometrical interpretation of the dimensionless stress, imagine that it is due solely to hydrostatic pressure  $P_0 = \rho g h$ . Thus, the stress is simply the ratio of the height  $h$  of the tube center above the flat surface of a liquid reservoir to the tube radius  $R_T$ . When the stress is negative, the tube center lies below the reservoir surface. For the case of fillets in a heat pipe with a slab wick, a third parameter, the ratio of the wick thickness  $T$  to the tube radius  $R_T$ , is required.

The results for a puddle are displayed in Figure 1.4 (a) - (d) for values of the Bond number of 0.1, 1., 10., and 100. For each Bond number, the puddle configuration, its area, free perimeter and wetted perimeter are shown for a range of stress. The puddle area is made dimensionless by dividing by the cross-sectional area of the tube, and the free and wetted perimeter are made dimensionless by dividing by the circumference. Thus we see that the dimensionless area and wetted perimeter approaches unity as the puddle nearly fills the tube. For high values of stress when the puddle is shallow, the free perimeter and wetted perimeter are nearly equal.



ORIGINAL PAGE IS  
OF POOR QUALITY

FOLDOUT FRAME /

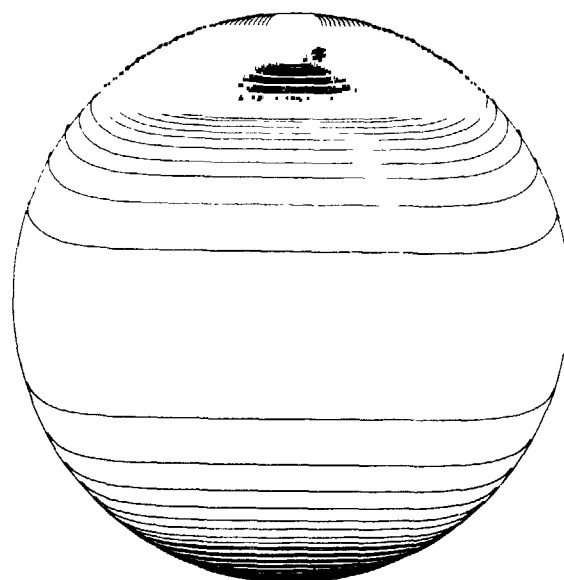
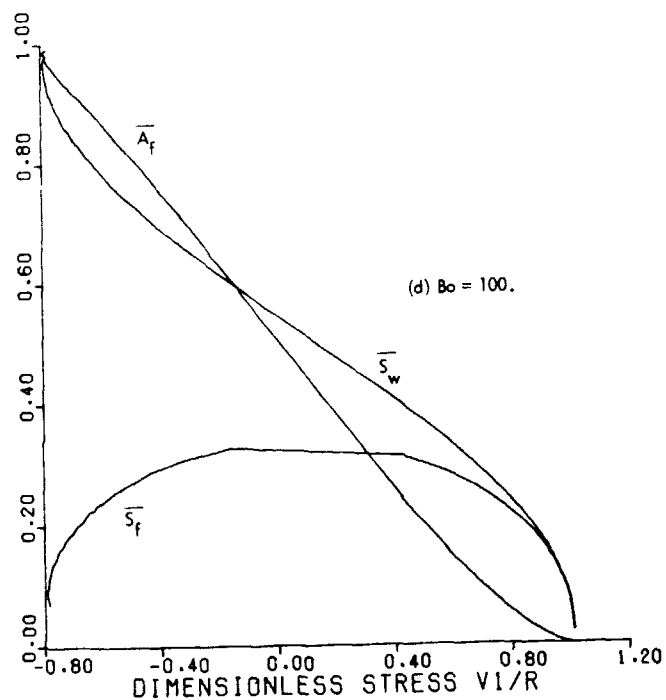
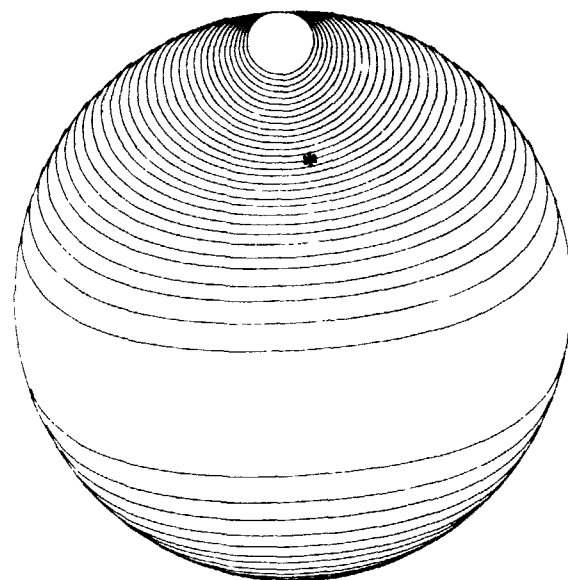
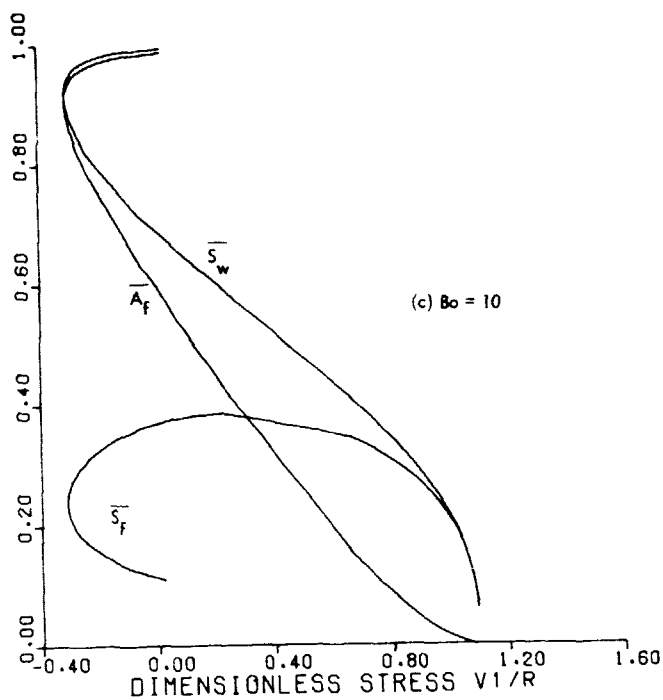


Figure 1-4. Fillet configurations in horizontal circular cylinders. Dimensionless fillet area  $\bar{A}$ , wetted perimeter  $\bar{S}_w$ , and free perimeter  $\bar{S}_f$  are plotted as a function of dimensionless stress  $V_1/R$ . An asterisk denotes the neutrally stable meniscus.



As will be discussed in the next section, those liquid configurations for which the fillet area increases with increasing stress are unstable and cannot exist. Note that this is the case for all puddle configurations when  $B = 0.1$ . The critical-free surfaces, which are neutrally stable are denoted in the figure. For stresses below the critical stress, a liquid slug forms.

## 1.2 EXCESS LIQUID SLUGGING OF VAPOR SPACES AND THE PRIMING OF ARTERIES

In this section we focus on the conditions under which a liquid slug forms in a vapor space, which, as mentioned previously, also applies to the priming of arteries. There are two distinct situations to consider; vapor spaces with and without solid end boundaries. The former occurs in most simple heat pipes, such as an axially grooved or a slab-wick heat pipe that have end caps. The latter occurs primarily in gas-loaded heat pipes where the condenser end protrudes into a gas reservoir and is otherwise uncapped. We consider this situation first.

### 1.2.1 Slugging of Open Vapor Spaces

Consider an experiment, as shown in Figure 1.5, where a horizontal open-ended porous tube is lowered into a liquid pool. The capillary stress is measured by the elevation  $h$  of the tube center above the pool. If the Bond Number is sufficiently large, a puddle of cross-sectional area  $A$  will form before the tube slugs with liquid. As  $h$  is decreased  $A$  increases. The tube will abruptly slug with liquid when  $dA/dh = \infty$ . This slugging criterion, shown in Figure 1-6 by the dashed line, is found from the calculations of the program FILLET such as those displayed in Figure 1-4. In Figure 1-6, instead of plotting the critical height to the center of the tube, we plotted the critical height to the top, which eliminates negative values and allows the use of logarithmic graph paper.

If the Bond number is sufficiently small, then  $dA/dh$  is positive for all puddles, and hence none are stable. Therefore, slugging abruptly occurs as soon as a puddle begins to form on the bottom of the tube. Such a puddle has a radius of curvature nearly equal to the tube radius and thus, by Eq. (1.1) the gas-liquid pressure difference at the tube bottom is  $\sigma/R_T$ :

$$\rho g (h - R_T) = \alpha / R_T,$$

or in dimensionless form

$$h/R_T - 1 = 1/B. \quad (1.29)$$

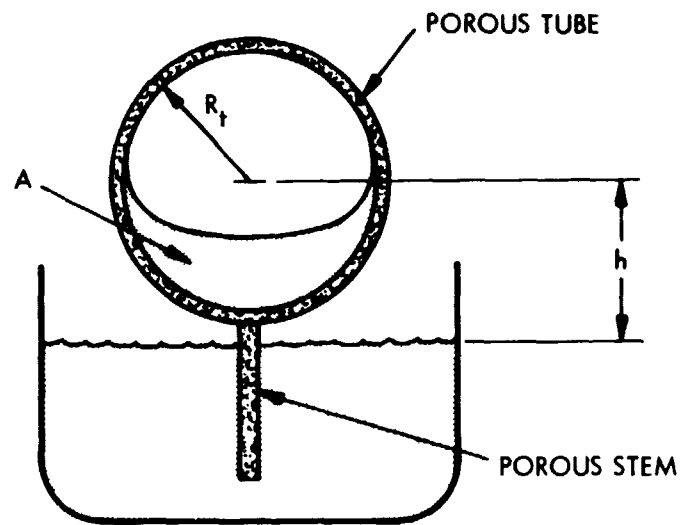


Figure 1-5. When the cylindrical tube is lowered sufficiently, a liquid slug will abruptly form.

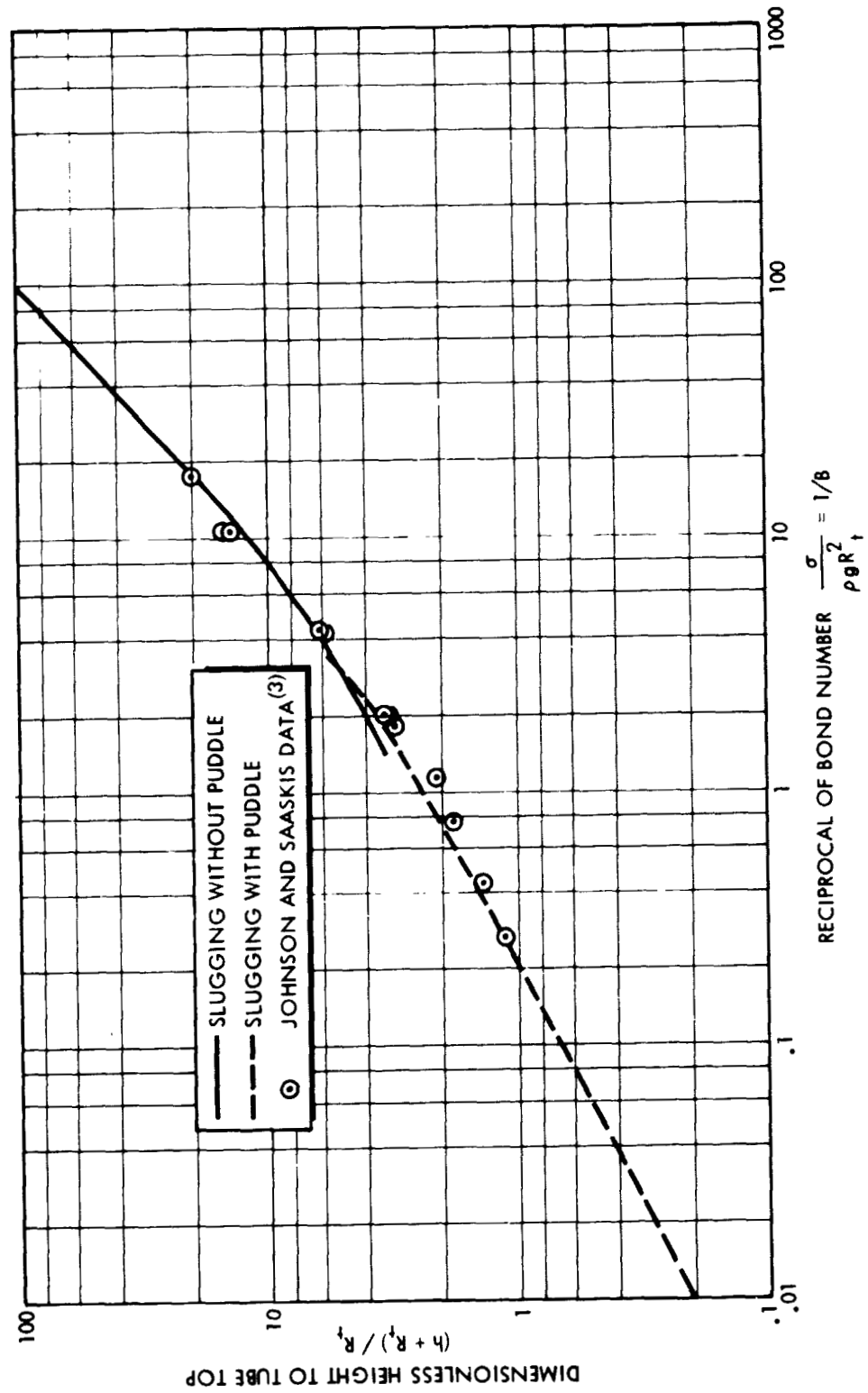


Figure 1-6. Slugging criterion for open-ended cylindrical tubes.

This criterion for slugging is displayed in Figure 1-6 by the solid line. The intersection of the dashed and solid lines at a Bond number of .33 represents the point at which a stable puddle is just possible. The analytical calculation of this critical Bond number poses an intriguing academic challenge. Also displayed in Figure 1-6 is data taken by Johnson and Saaski<sup>(3)</sup> on the priming of open-ended glass and screen walled tubes ranging from 0.51 mm to 3.2 mm with 2-propanol and Freon 113 as the liquid.

The condition for open-ended slugging of "Dee-shaped" vapor spaces can also be found by the program FILLET, which calculates the fillet areas  $A_f$  as a function of stress  $S$ . Slugging occurs when one of the two fillets, or the puddle if one is possible, becomes unstable, that is  $dA_f/dS = \infty$ .

### 1.2.2 Slugging in a Closed Vapor Space

In a vapor space with a closed end, a slug first begins to form at the end, and then grows progressively longer. Such a slug is depicted in Figure 1-7. The closed-vapor-space slugging criterion is more important than the open criterion, therefore, in this section we present detailed results for the "Dee" shape as well as the circular vapor space.

The critical capillary stress for the formation of a slug is higher for the closed vapor space owing to the fact that the free surface develops curvature in two orthogonal planes rather than just one. In fact, if the stress is sufficiently low for a liquid slug to form in an open vapor space, then to clear the slug the stress must be increased to the critical stress for slugging of the closed vapor space. For example, in the design of a graded-porosity wick, even if the condenser end opens into a gas reservoir, the slugging criterion for a closed vapor space should be used, because the condenser-end porosity must be low enough to generate a sufficient capillary pressure to clear an existing slug. Similarly, while the maximum stress to initiate priming of an open artery is set by the slugging criterion for open vapor spaces, the capillary pumping, that is, the stress necessary to initiate emptying, is set by the slugging criterion for closed vapor spaces.

The mathematical modeling of the slug that forms in the closed vapor space is difficult because the free surface varies in three dimensions. We consider first the circular vapor space and employ an approximation suggested by Johnson and Saaski<sup>(3)</sup> to reduce the problem to a two-dimensional one. Applying Eq. (1.1) to the free surface shown in Figure 1.7, we take  $R_1$  as the local radius of curvature in the y-z plane which bisects the tube vertically and  $R_2$  as the local radius of curvature in plane orthogonal to the y-z plane that contains the local normal to the surface. The approximation is to use a constant characteristic value for  $R_2$ , and for lack of a better candidate this constant value is taken as the tube radius  $R_T$ . The equation governing the meniscus shape in the z-y plane is developed exactly the same as Eqs. (1.5) and (1.6), except the constant term  $1/R_T$  is carried along. Thus, instead of Eq. (1.6), we obtain

$$(2y - 1/R_T) \frac{dy}{d\alpha} = a^2 \sin \alpha \quad (1.30)$$

Referring to Figure 1.7, we see that the boundary conditions for the free surface curve is

$$\alpha = 0 \text{ at } y = h - R_T + d$$

and (1.31)

$$\alpha = -\pi \text{ at } y = h + R_T$$

In case slugging occurs without a puddle forming first, we take  $d = 0$ . Integration of Eq. (1.30) between the above boundary conditions results in

$$d^2 + d[2h - 2R_T - a^2/R_T] + 4[a^2 - R_T h] = 0 \quad (1.32)$$

The no-puddle slugging condition is ( $d = 0$ )

$$h/R_T = 2/B \quad (1.33)$$

Equation (1.29) gives the condition for a puddle just about to form. The two curves given by Eqs. (1.29) and (1.33) intersect at  $B = 1$ . Thus, for  $B < 1$ , the slug forms without a puddle and Eq. (1.33) is the appropriate criterion. For  $B > 1$ , we use a modification of the program FILLET to calculate the puddle depth as a function of  $h/R_T$  and  $B$ :

$$d/R_T = f(h/R_T, B) \quad (1.34)$$

This relation is used to eliminate  $d$  from Eq. (1.32). The resulting slugging criterion for  $B > 1$  along with the criterion for  $B < 1$  given by Eq. (1.33) are displayed in Figure 1.8.

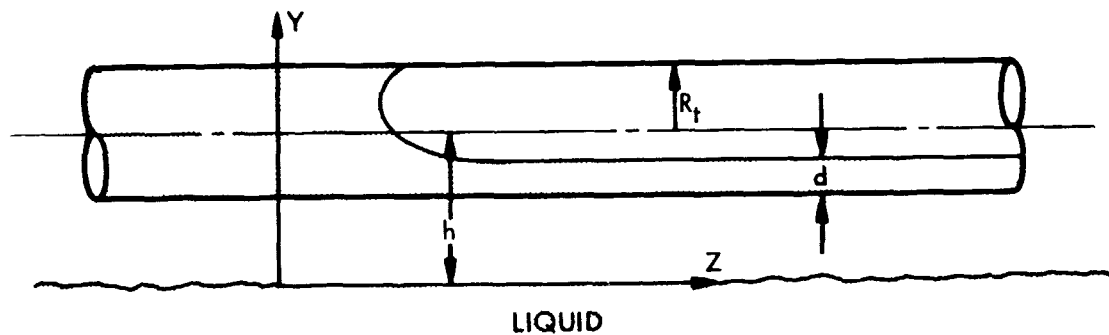


Figure 1.7. Liquid Slug with a Puddle of Depth  $d$  on the Bottom of the Tube

The validity of the approximation of Johnson and Saaski can only be assessed by comparing the resulting slugging criterion to experimental results or to an exact numerical solution. We carried out an experiment with a series of glass tubes that varied in diameter from 2 to 30 mm. As shown in the Figure 1.9, one end of each tube was drawn down to half the original diameter and the tapered section was bent 90°. The set of tubes were placed on a level platform inside a large glass jar with the tapered sections down. The jar was slowly filled with acetone. At a critical level, a liquid slug, which initiated in the tapered section, moves rapidly through the smallest tube. The height of the critical level is measured with a cathetometer. The jar is slowly filled again until the slug moves through the second tube, and the height is measured again, and so forth. From these data, the critical values for  $h$  can be calculated for each tube.

The experimental results are displayed in Figure 1.8. There is excellent agreement except at large values of  $B$ , where the theory under

under-predicts the critical stress. One expects this, because at these large values of  $B$  the puddle itself nearly fills the tube before slugging occurs. As seen in Figure 1.4(d), when the puddle level is near the top, the transverse radius of curvature  $R_2$  is on the average much smaller than the tube radius  $R_T$  that is used to approximate it in the theory.

The slugging criterion for "Dee-shaped" vapor spaces was measured experimentally for shapes corresponding to a typical ratio of the wick thickness to tube diameter of 0.465. Long stainless-steel strips of the appropriate width were inserted into each glass tube and held in place with a spring. Slugging of the resulting "Dee-shaped" vapor space was measured with the "Dee" on the top and the bottom, which corresponds to a horizontal wick, and on the side, which corresponds to a vertical wick. The results are displayed in Figure 1.10. In the case of the "Dee," the Bond number is based on one-half of the hydraulic diameter  $D_h$  instead of the tube radius. The faired lines through the data of Figure 1.9 are given by an empirical data fit

$$h_T/D_h = \frac{1}{B} + \frac{\alpha}{B^\beta} (1 - \eta e^{-\gamma\sqrt{B}})$$

where the empirical constants are given in Table 1.1. These empirical results are incorporated in the computer program GRADE<sup>(4)</sup> so that optimum graded-porosity wicks can be designed that just prevent the occurrence of a liquid slug.

Table 1.1. Constants for the Empirical Curve Fit for the Slugging Condition for "Dee-Shaped" Vapor Spaces				
$h_T/D_h = 1/B + (\alpha/B^\beta)(1 - \eta e^{-\gamma\sqrt{B}})$				
	$\alpha$	$\beta$	$\gamma$	$\eta$
Dee on top	.820	.40	1.5	2.9
Dee on bottom	.68	.40	1.5	1.9
Dee on side	1.5	.5	1.0	1.2

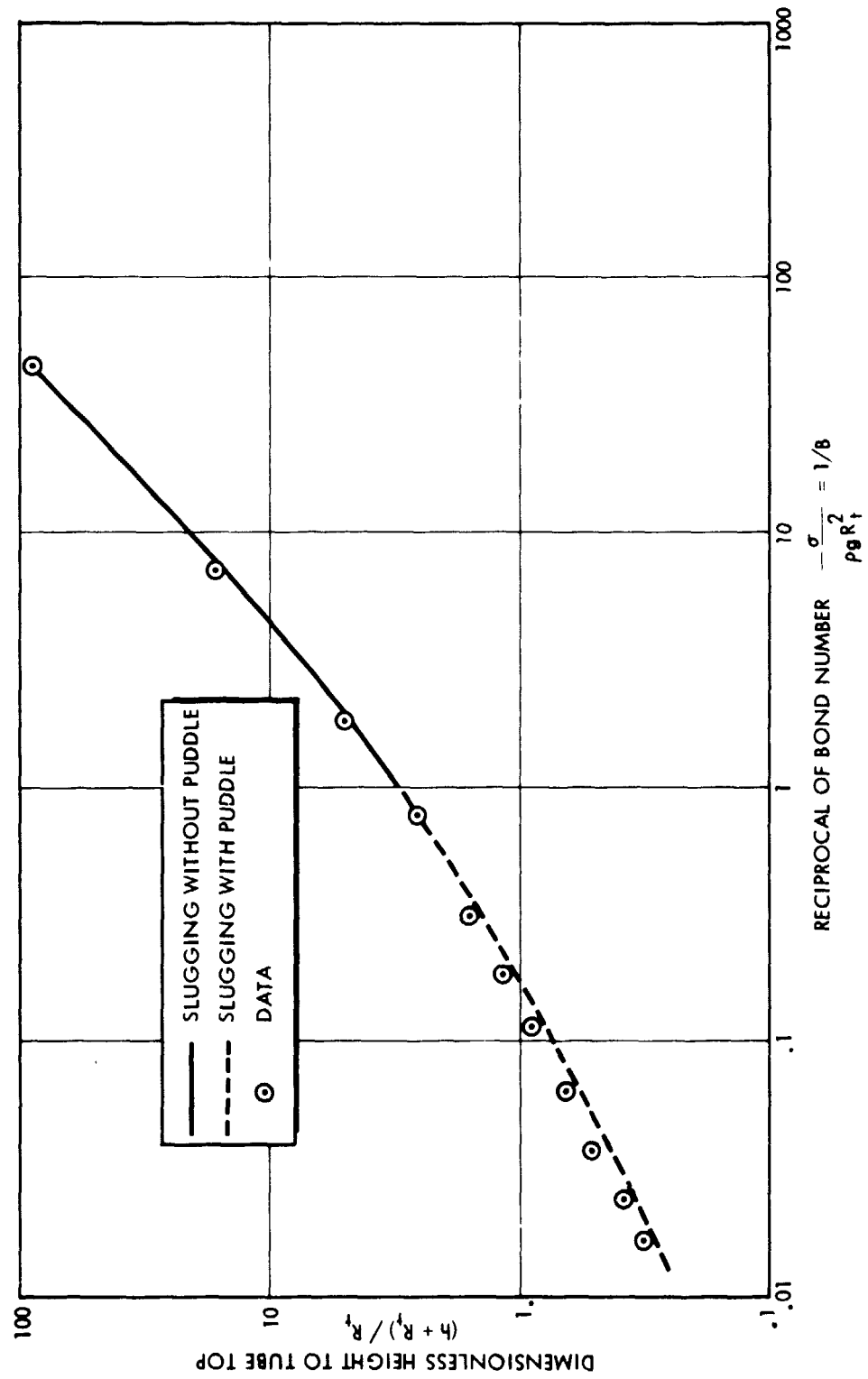


Figure 1.8. Slugging Criterion for Closed-Ended Cylindrical Tubes



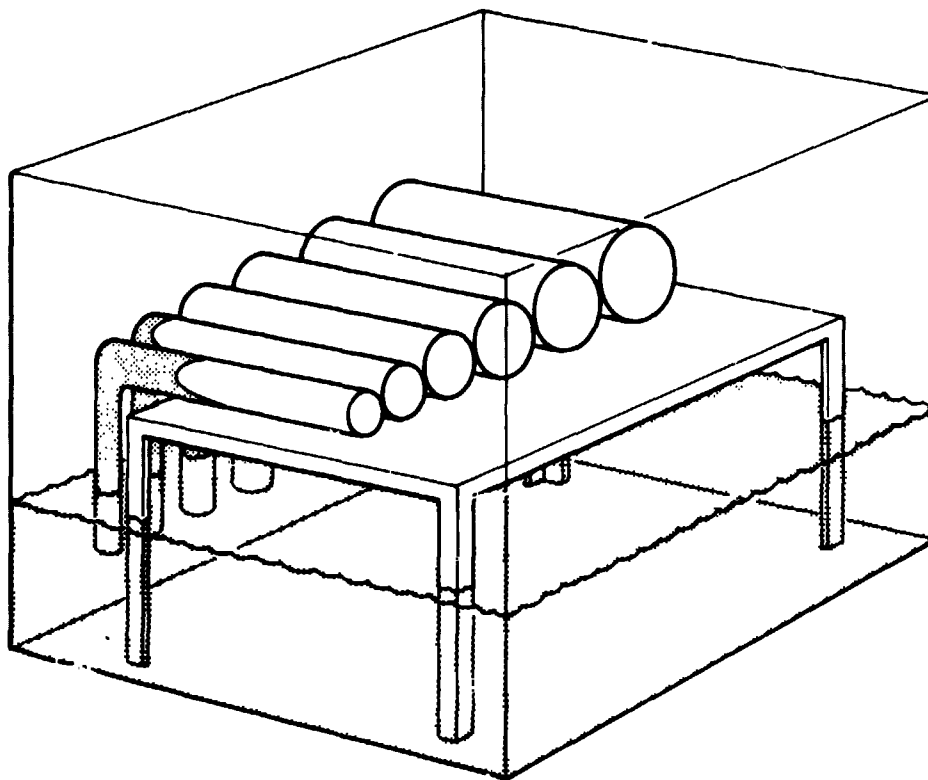


Figure 1.9. Schematic Diagram of Apparatus to Measure the Slugging Criterion for Closed-Ended Cylinders. Slug is shown formed in the smallest tube.

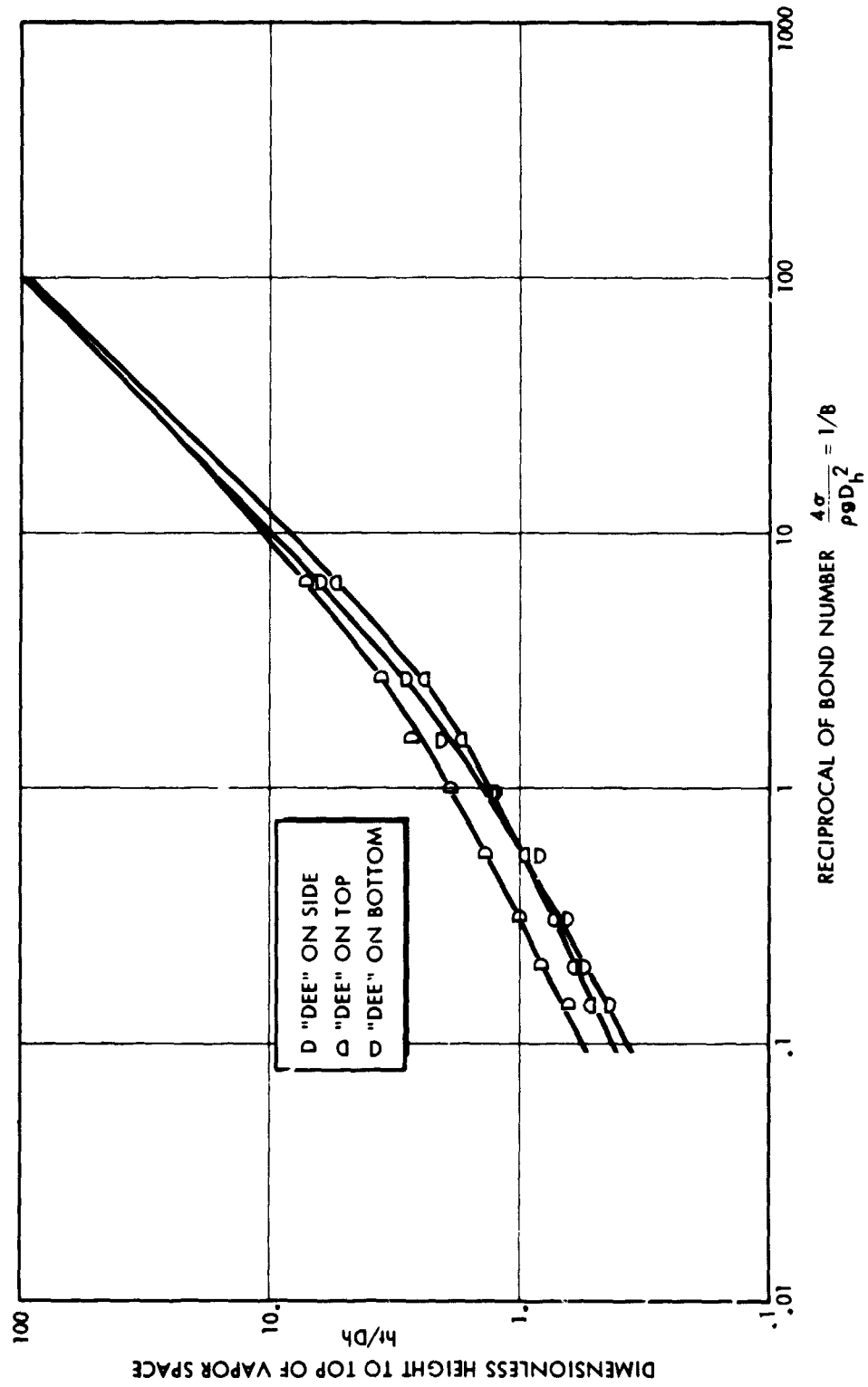


Figure 1.10. Empirical Sluaging Criterion for "Dee-Shaped" Vapor Spaces

## 2.0 THE CAPACITY OF CIRCUMFERENTIAL GROOVES

Many heat pipes use a wick structure for the axial transport of liquid, and circumferential grooves for the transport across the inner tube wall in the evaporator and condenser regions. This combination provides both high axial transport and heat-transfer coefficients. Our particular interest is the use of circumferential grooves with the graded-porosity slab wick; however, the results of this section apply to any heat pipe that uses circumferential grooves.

A sound mathematical model of circumferential grooves is required for the program GRADE<sup>(4)</sup>, which designs graded-porosity wicks, because the evaporator grooves are the limiting factor for the transport capacity. GRADE repeatedly integrates the governing differential equations. Each integration uses an assumed value for the axial heat-transport rate, and a subroutine DRY reports whether the circumferential grooves fail. If they do, the assumed heat-transport rate is reduced, and if they don't the rate is increased. Then the integration is repeated. A binary search on the rate is used to design a graded-porosity wick with the highest axial heat-transport capacity that will not fail the circumferential grooves.

In this section, we present the mathematical model for the subroutine DRY. The method used is similar to that used by Gier and Edwards<sup>(5)</sup>, except that here the more general trapezoidal groove rather than the triangular groove is considered, and a general wick structure is considered rather than one that feeds the grooves only at the bottom.

Figure 2.1 depicts the geometry under consideration. To be specific, a vertical slab wick is shown. However, the method applies to any wick configuration. We focus attention on a single region of grooves that is fed liquid from the wick at angular locations  $\theta_1$  and  $\theta_2$  that are measured from the top (positive in the counterclockwise direction). The total heat input per unit length along the heat pipe is  $Q$ , and a fraction  $F_Q$  is assumed to enter between  $\theta_1$  and  $\theta_2$ .

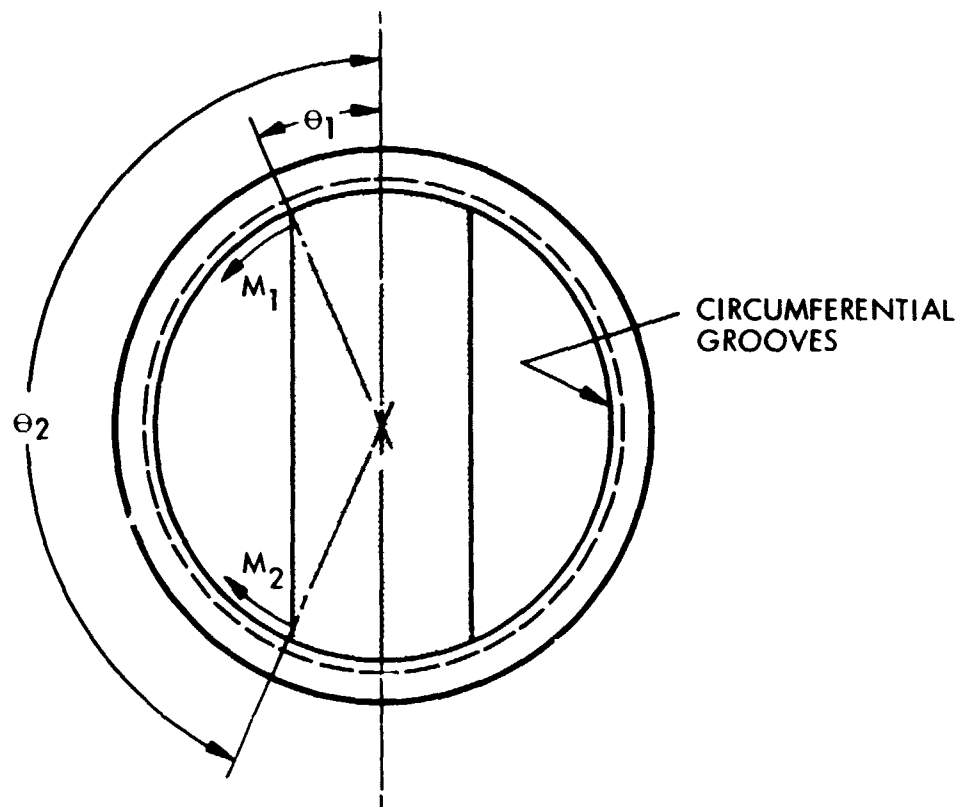


Figure 2.1. Liquid Enters a Groove at the Rate  $M_1$  at Location  $\theta_1$  and at the Rate  $M_2$  at Location  $\theta_2$ . It is uniformly evaporated between  $\theta_1$  and  $\theta_2$ .

We assume that the heat is evaporated uniformly along the groove, thus the amount of liquid evaporated between location  $\theta$  and  $\theta+d\theta$  is

$$d\dot{m}(\theta) = -(F_Q Q/\lambda N) [d\theta/(\theta_2-\theta_1)] \quad (2.1)$$

where  $\dot{m}(\theta)$  is the local mass flow through the groove assumed positive in the counterclockwise direction,  $N$  is the number of grooves per unit length and  $\lambda$  is the latent heat. Integration of Eq. (2.1) over the interval  $(\theta_1, \theta_2)$  yields

$$(m_1 + m_2) = F_Q \dot{Q}/\lambda N \quad (2.2)$$

where  $m_1$  and  $m_2$  are the absolute values of the flow rates into the groove at  $\theta_1$  and  $\theta_2$ . One location  $\theta_s$  between  $\theta_1$  and  $\theta_2$  is a stagnation point where the flow rate is zero. By integrating Eq. (2.1) from  $\theta_1$  and then  $\theta_2$  to  $\theta_s$ , we obtain the result

$$m_1/m_2 = (\theta_s - \theta_1)/(\theta_2 - \theta_s) \quad (2.3)$$

Unless the region of grooves under consideration is situated symmetrically in a gravitational field or they are operating in zero gravity, in which case  $m_1$  equals  $m_2$ , then one does not know *a priori* the values of  $m_1$  and  $m_2$ . Their sum is given by Eq. (2.2) and the unknown location of the stagnation point fixes their ratio by Eq. (2.3). Combining these equations we obtain expressions for  $m_1$  and  $m_2$  in terms of  $\theta_s$ :

$$m_1 = (F_Q \dot{Q}/\lambda N) (\theta_s - \theta_1)/(\theta_2 - \theta_1), \quad (2.4)$$

$$m_2 = (F_Q \dot{Q}/\lambda N) (\theta_2 - \theta_s)/(\theta_2 - \theta_1). \quad (2.5)$$

Thus our lack of knowledge of the values of  $m_1$  and  $m_2$  is shifted to the unknown location  $\theta_s$  of the stagnation point. Integrating Eq. (2.1) from  $\theta$ , with the use of Eq. (2.4) we obtain for the mass flow rate

$$\dot{m}(\theta) = (F_Q Q/\lambda N) (\theta_s - \theta)/(\theta_2 - \theta_1) \quad (2.6)$$

As liquid flows through the groove, its pressure drops relative to that of the vapor. The pressure difference is sustained by the curvature of the free-surface meniscus. The rate of increase of the liquid-vapor pressure difference  $P$  is governed by the expression

$$\frac{dP}{d\theta} = - R_T \frac{K}{R_e} (1/2 \rho U^2)/D_h - \rho g R_T \sin \theta \quad (2.7)$$

where  $R_T$  is the inside radius of the tube  
 $K$  is the friction-factor coefficient  
 $R_e$  is the Reynolds number based on the hydraulic diameter  $D_h$   
 $\rho$  is the liquid density  
 $U$  is the average liquid velocity.

In terms of the mass flow rate given by (2.6), we write

$$\frac{dP}{d\theta} = \frac{R_T K v}{2D_h^2 A} (F_Q Q/\lambda N)(\theta_s - \theta)/(\theta_2 - \theta_1) - \rho g R_T \sin \theta \quad (2.8)$$

This equation must be integrated numerically because  $K$ ,  $D_h$ , and  $A$  vary depending on the shape of the meniscus, which in turn depends on  $P$ . Since typically the Bond number is very small, we assume that the meniscus is circular, and thus the liquid in the grooves is as shown in Fig. 2.2. The radius is given in terms of the local liquid-vapor pressure difference  $P$  and surface tension  $\sigma$  by:

$$R = \sigma/P \quad (2.9)$$

When the vapor-liquid pressure difference is low, the meniscus is attached to the top of the groove. As the pressure difference increases, the radius of curvature of the meniscus decreases. When the contact angle  $\lambda$  reaches the wetting angle  $\alpha$ , a further increase in the pressure difference results in the meniscus receding into the groove as shown in Fig. 2.2(b). Groove failure is taken to occur when the meniscus reaches the groove bottom.

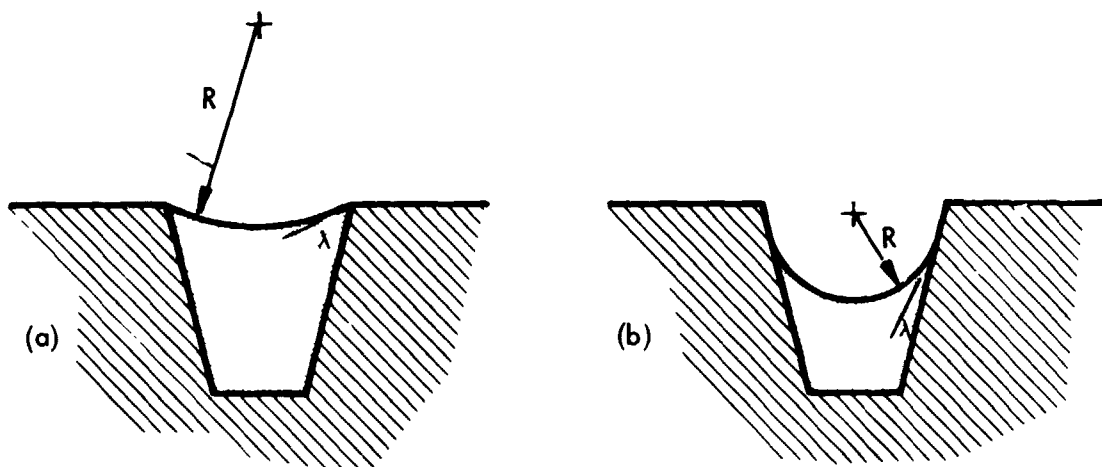


Figure 2.2. Cross Section of a Groove  
 (a) Meniscus of liquid attached to top of groove with contact angle  $\lambda$ .  
 (b) Meniscus receded into groove (contact  $\lambda$  equals wetting angle  $\alpha$ ).

The area  $A$  and hydraulic diameter  $D_h$  are easily calculated for a given value of  $P$  once  $R$  is calculated from Eq. (2.9). For the calculation of the friction factor coefficient, we rely on the work by Hsu<sup>(6)</sup> who used numerical techniques to calculate the friction factor for a circular meniscus in a trapezoidal groove. The subroutine DRY contains a subroutine FACTOR that is devoted to producing an empirical curve fit to Hsu's numerical results.

The boundary conditions for Eq. (2.8) are the values of the vapor-liquid pressure difference at the two feed locations, which are related hydrostatically to the stress  $S$  at the tube center;

$$\begin{aligned} P_1 &= S + \rho g R_T \cos \theta_1 , \\ P_2 &= S + \rho g R_T \cos \theta_2 , \end{aligned} \quad (2.10)$$

Equation (2.8) with the boundary conditions (2.10) constitute a two-point boundary-value problem where the unknown stagnation point  $\theta_s$  is an eigenvalue. One can attempt a solution by repeatedly integrating from  $\theta_1$  to  $\theta_2$ , each time adjusting the value of  $\theta_s$  until both boundary conditions are met. A solution will be possible if the heat input  $Q$  is below the critical value at which the groove fails. Such an iterative search for a solution is time consuming, especially when the computer subroutine that would carry it out is itself called repeatedly. It is often possible to decide whether or not  $Q$  is above the critical value based on a single integration. Consider a curve constructed as follows. We assume a value for  $\theta_s$  and then integrate Eq. (2.8) from  $\theta_1$  to  $\theta_s$ . In Fig. 2.3 we plot the vapor-liquid pressure difference  $P_s$  at the stagnation point as a function of  $\theta_s$ . The curve ends when  $P_s$  is sufficiently high to fail the groove. Similarly, we integrate from  $\theta_2$  to  $\theta_s$  and again plot  $P_s$  as a function of  $\theta_s$ . If  $Q$  is below the critical value for groove failure, the two curves will intersect at the actual stagnation point, as shown in Fig. 2.3(a). If, on the other hand,  $Q$  is above the critical value, they will not intersect as shown in Fig. 2.3(b).

We now can describe the procedure used to assess whether or not the groove has failed. A trial value of  $\theta_s$  is assumed half way between  $\theta_1$  and  $\theta_2$ , and we attempt to integrate to it first from  $\theta_1$  and then from  $\theta_2$ . If



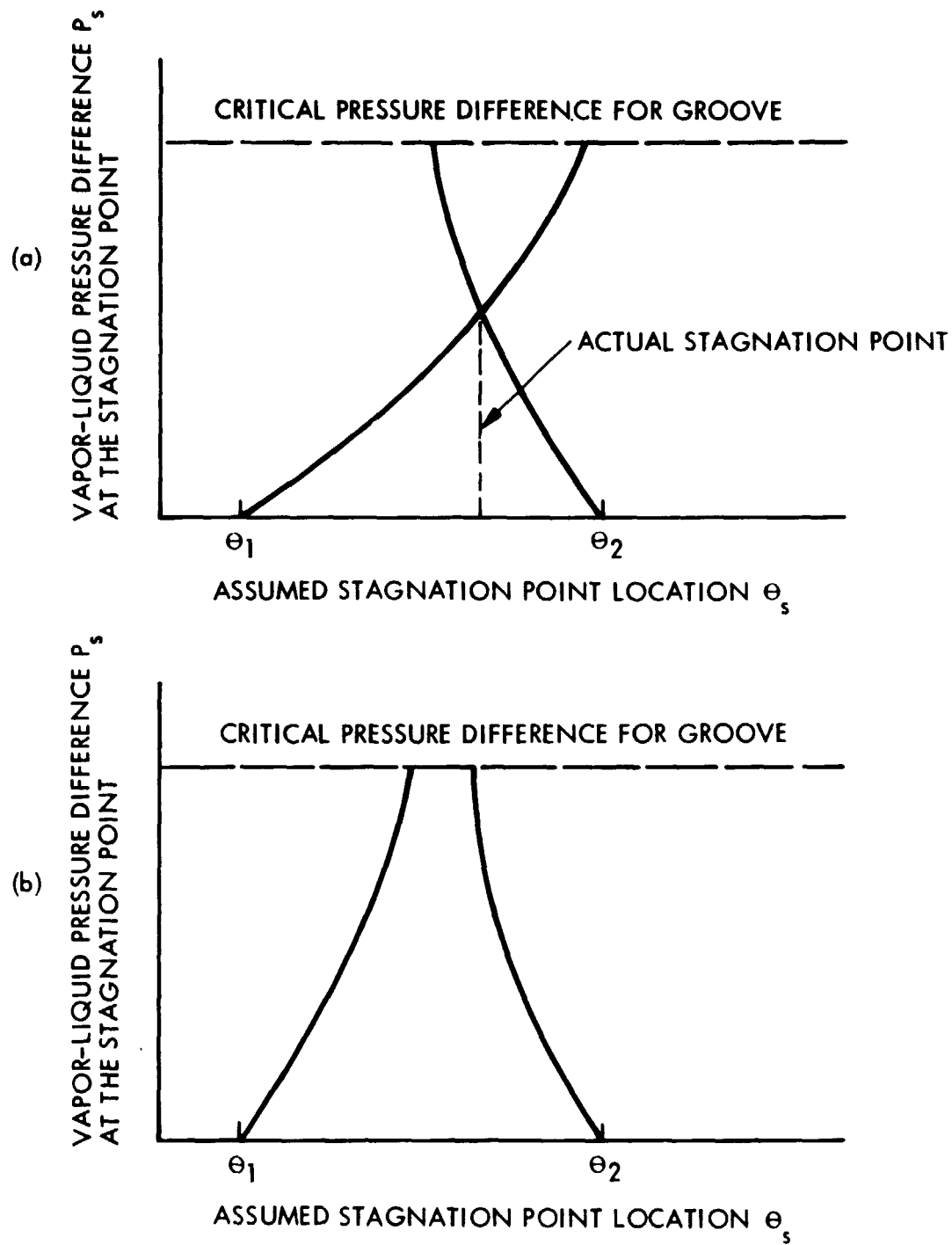


Figure 2.3. Plots of the Vapor-Liquid Pressure Difference at an Assumed Stagnation Point Location  $\theta_s$  by Integrating from Both  $\theta_1$  and  $\theta_2$  to  $\theta_s$ . (a) Case where grooves function, (b) Case where they dry out.

two values of  $P_g$  are successfully calculated without groove failure, then even if they are not the same we have demonstrated that the two curves are as in Fig. 2.3(a) and they must intersect. Therefore, we conclude that the groove has not failed. If both attempts to integrate to  $\theta_g$  fail, then we have demonstrated that the two curves are as in Fig. 2.3(b) and they do not intersect. Therefore, we conclude that the groove has failed. Only when integration to the trial value for  $\theta_g$  is successful from one direction but not from the other, can we draw no conclusion. When this happens, a new trial value for  $\theta_g$  is selected, and the procedure is repeated until a conclusion can be drawn. Usually only a few tries are needed at most.

The procedure just described is incorporated in the computer subroutine DRY, which reports whether the grooves have failed for a given heat input and capillary stress at the tube center. Sample results are shown in Fig. 2.4. The primary input to DRY, besides parameters describing the groove geometry and fluid properties, is the heat input per unit length of heat pipe  $Q_L$  and the capillary stress, which is specified by the radius of curvature  $R_{cap}$  of the free surface in a groove under the capillary stress  $S$ :

$$S = \sigma/R_{cap}.$$

The region above the curve in Fig. 2.4 corresponds to values of  $R_{cap}$  and  $Q_L$  where the grooves are failed, while the region below it corresponds to values where the grooves are not failed.

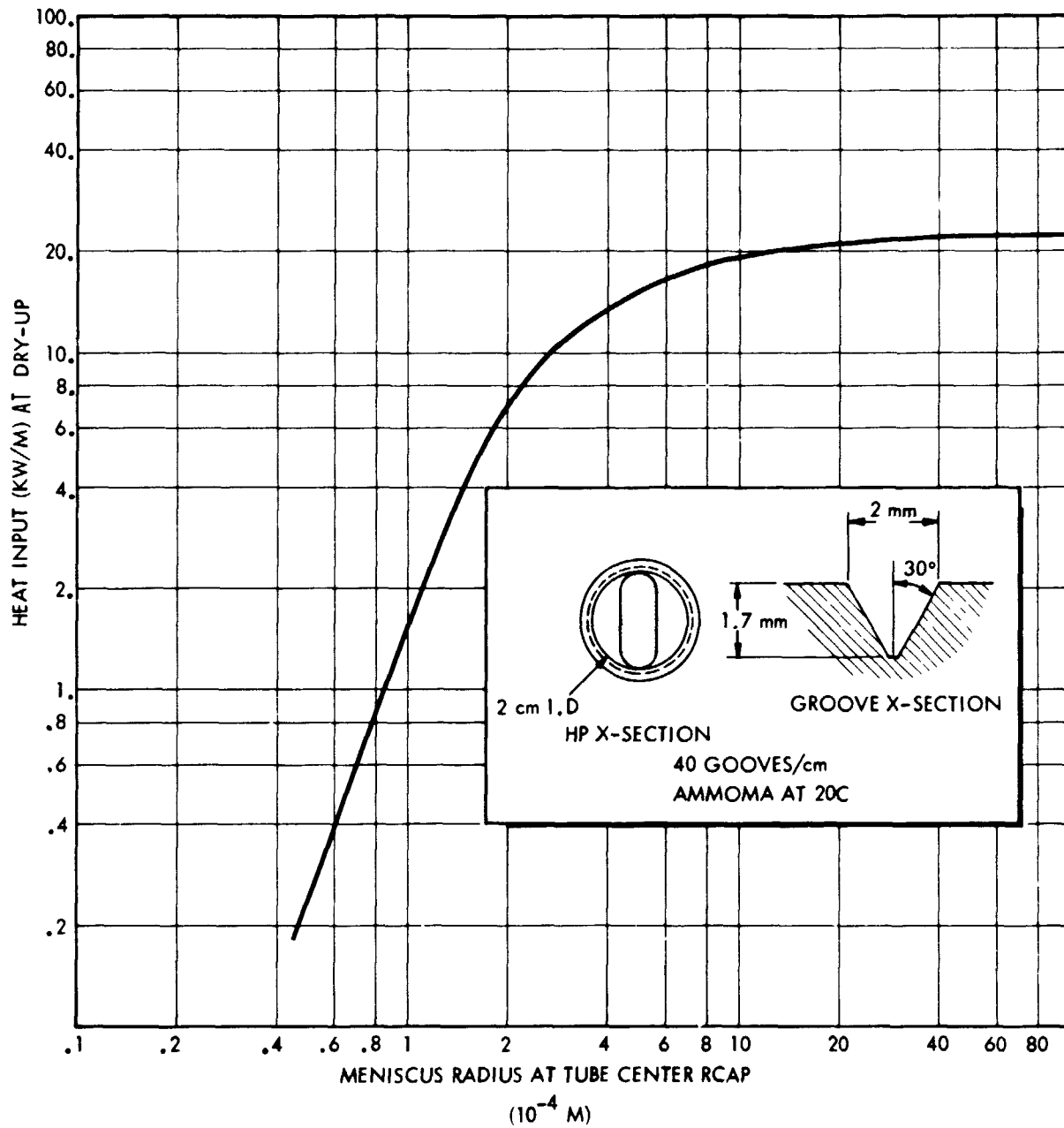


Figure 2.4. Sample of Groove Dryout Calculations

### 3.0 VAPOR FLOW IN HEAT PIPES

We consider in this section the effect of vapor flow on wick-limited heat pipes. Vapor flow is often an important design consideration since the vapor-liquid pressure difference that must be supported by the capillary pressure of the wick is the sum of the pressure drop in the vapor as well as in the liquid. If a heat pipe has a negligible vapor-flow pressure drop at its maximum heat-transport rate, then it is often possible to increase its capacity by increasing the cross-sectional area of the wick. In the limit of this process where the wick completely fills the heat-pipe cross section, the capacity, of course, falls to zero. Therefore, an optimum cross-sectional area for the wick exists and when other factors such as radial heat transfer and vapor-space slugging are not a consideration, this optimum occurs when the vapor-flow and liquid-flow pressure drops are of the same magnitude. An accurate calculation of the vapor-pressure profile is especially important for a graded-porosity wick because it is designed to just sustain the vapor-liquid pressure difference along its length rather than only at the evaporator end.

The vapor-flow calculation is difficult because heat pipes often operate in a regime where there is an essential interaction between viscous and inertial forces. This has been the subject of considerable study which has been reported in the literature. Bankston and Smith<sup>(7)</sup>, and Tien and Rohani<sup>(8)</sup>, for example, resorted to a numerical solution of the full Navier-Stokes equations, while Busse<sup>(9)</sup>, Galowin et al<sup>(10,11)</sup>, Quail and Levy<sup>(12,13)</sup> and Gupta and Levy<sup>(14)</sup> based their analysis on the boundary-layer equations. Their solutions are limited to either circular, plane-parallel or annular vapor-space cross sections. We are primarily interested in, rather, the "Dee-shaped" vapor space formed by a graded-porosity slab wick in a circular tube. Also, the mathematical complexity of the solution of either the Navier-Stokes or the boundary-layer equations makes such an approach unsuitable for routine computer-design calculations. In section 3.1 we present a simplified approximate mathematical model that is based on the results of earlier more exact theories. It has the virtue of providing a fast calculation of the

static-pressure profile of the vapor in a Dee-shaped vapor space while retaining the effect of the inertial-viscous interaction. In section 3.2, we present the results of an experiment that actually measures the pressure profile in the vapor.

### 3.1 THEORETICAL MODEL FOR VAPOR FLOW IN A DEE-SHAPED SPACE

#### 3.1.1 Flow in the Adiabatic Section

A rigorous analysis of the actual Dee shape would require at least a three-dimensional solution of boundary-layer equations, which is far beyond the scope of a design-oriented subroutine. Therefore, as our first step we approximate the Dee shape by a two-dimensional configuration that consists of two flat parallel plates. One is always adiabatic and models the surface of the wick. The other, which models the tube wall, is either a surface of evaporation, condensation, or it is also adiabatic. A question arises as to the plate separation that will best approximate a Dee-shape. The criterion that is used requires that the flow in both the actual Dee-shaped passage and between the parallel walls have the same average velocity and the same pressure gradient  $dP/dx$  in adiabatic regions of fully developed flow. If we let the subscript ( )<sub>D</sub> refer to the Dee-shape and ( )<sub>||</sub> refer to the parallel plates, then the criterion for the plate spacing is

$$\frac{dP}{dx} = \frac{96}{Re_{||}} \frac{1/2 \rho u^2}{D_{||}} = \frac{(f_D \cdot Re_D)}{Re_D} \frac{1/2 \rho u^2}{D_D} \quad (3.1)$$

where  $f_D$  is the friction factor,  $Re$  is the Reynolds number based on the hydraulic diameter  $D$ ,  $\rho$  is the vapor density and  $u$  is the average velocity. After we have substituted twice the plate spacing  $b$  for the hydraulic diameter of parallel plates, equation (3.1) reduces to

$$b = 2 \sqrt{6/f_D Re_D} D_D \quad (3.2)$$

The friction factor  $f_D$  depends on the ratio of wick thickness to tube diameter, and in general it must be found from the numerical solution of Poisson's equation:

$$\frac{dp}{dz} = \mu \left( \frac{\partial^2 u}{\partial x^2} + \frac{\partial^2 u}{\partial y^2} \right), \quad (3.3)$$

where here the  $z$  axis is taken as the flow direction,  $x$  and  $y$  are transverse coordinates,  $u$  is the flow velocity,  $p$  is the pressure and  $\mu$  is the viscosity. Equation (3.3) is written in dimensionless form by introducing the dimensionless variables

$$U = -u \left( \frac{dp}{dz} \frac{d^2}{\mu} \right), \quad (3.4)$$

$$X = x/d, \quad (3.5)$$

$$Y = y/d, \quad (3.6)$$

where  $d$  is the tube diameter, and we obtain,

$$\frac{\partial^2 U}{\partial X^2} + \frac{\partial^2 U}{\partial Y^2} = -1. \quad (3.7)$$

The boundary conditions require  $U$  to vanish on the boundary. Once we obtain a solution, the friction factor is related to the average dimensionless velocity  $U_{ave}$  by

$$f_D Re_D = 2/U_{ave}. \quad (3.8)$$

Equation 3.7 is written in a finite-difference form by overlaying the flow region on an  $N \times N$  rectangular grid. By symmetry, only half of the region must be used. Solution for the velocity  $U_{ij}$  at the  $(i,j)$  node is obtained by Gauss-Seidel iteration of the finite difference approximation to Eq. (3.7). The resulting friction-factor is shown in Figure 3.1.

Analytical results are possible for  $w/d = 0$  and asymptotically for  $w/d \rightarrow 1$ . The result of  $f_D Re_D = 62.8$  for  $w/d = 0$  is a special case of an analysis by Sparrow<sup>(15)</sup>. An asymptotic solution is possible in the

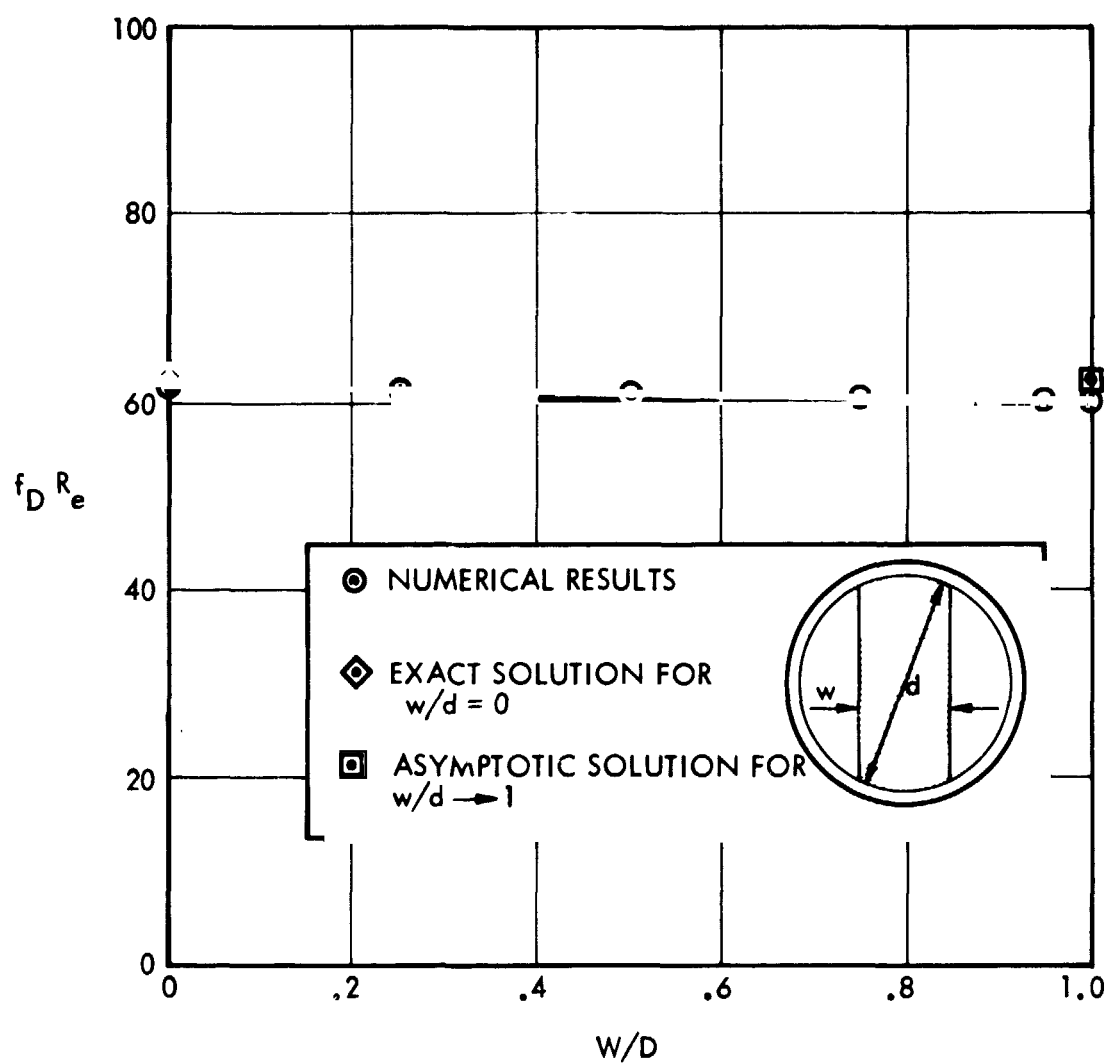


Figure 3.1 Friction-Factor For A "Dee-Shaped" Conduit

limit  $w/d \rightarrow 0$  because in Eq. (3.7)  $\partial^2 U / \partial Y^2$  can be neglected. The resulting friction factor is

$$\lim_{w/d \rightarrow 0} f_D Re_D = 590/9 = 62.2 \quad (3.9)$$

The numerical solution in Fig. 3.1 does not quite agree with the analytical results for  $w/d = 0$  and 1. This is attributed to the approximation of the exact differential equation by the finite difference equation. In fact, the friction factors shown in Fig. 3.1, which were calculated for a  $30 \times 30$  mesh, increased somewhat as a finer mesh was used.

We were surprised to find that the friction-factor is practically independent of  $w/d$ . For practical calculations, the average of the analytical results for  $w/d = 0$  and  $w/d = 1$  is recommended. This value is  $62.5/Re_D$ .

### 3.1.2 Flow in Condensing Sections

In the condensing section the continual loss of mass flow to the condenser wall requires a deceleration of the main flow which is brought about by a positive pressure gradient in the direction of flow. The positive pressure gradient tends to cause a flow reversal near the wall, where viscosity brings the tangential velocity to a low value so that inertia effects are overcome by the positive pressure gradient. This behavior is particularly true near a noncondensing surface, such as that of the slab wick. The tendency toward flow reversal lowers or indeed reverses the viscous shear stress which otherwise acts against the flow.

Consider an element  $dz$  long of a heat pipe with walls forming a cylinder in the general mathematical sense, i.e., parallel wall elements but not necessarily with a circular cross-section. A force-momentum balance requires the following:

$$\frac{d}{dz} \int_A \rho u^2 dA_C = - \frac{d}{dz} \int_A p dA_C - \int_C \tau_w dC \quad (3.10)$$

where  $A$  is cross-sectional area,  $\tau_w$  is wall shear stress and  $C$  is perimeter. The area-integrated terms will be written as overscored



quantities as follows

$$\int_A \rho u^2 dA \equiv \overline{\rho u^2} A \quad (3.11)$$

$$\int_A p dA \equiv \bar{p} A \quad (3.12)$$

Additionally, a velocity-squared shaped factor is introduced

$$F_s \equiv \overline{u^2} / \bar{u}^2 \quad (3.13)$$

A circumferentially averaged friction factor  $f$  (not to be confused with friction-factor coefficient to follow) is defined:

$$\int_C \tau_w dC = C \frac{f}{8} \rho \bar{u}^2 \quad (3.14)$$

Hydraulic diameter is also introduced

$$D = 4 A / C \quad (3.15)$$

With these definitions Eq. (3.10) takes the form

$$\frac{d\bar{p}}{dz} = - \frac{d}{dz} (F_s \rho \bar{u}^2) - \frac{f}{D} \frac{1}{2} \rho \bar{u}^2 \quad (3.16)$$

Equation (3.16) can be integrated over an entire length of a condenser with closed end at  $x = L$  to yield

$$p_L - p_0 = F_{s,0} \rho \bar{u}_0^2 - \int_0^L \frac{f(z)}{D} \frac{1}{2} \rho \bar{u}^2 dz \quad (3.17)$$

For a condenser with a uniform rate of condensation

$$\bar{u}(z) = \bar{u}_0 [1 - z/L] \quad (3.18)$$

Hence, Eq. (3.17) becomes

$$p_L - p_0 = F_{s,0} \rho \bar{u}^2 - \frac{L}{2D} \rho \bar{u}_0^2 \int_0^1 f [1-\xi] d\xi \quad (3.19)$$

where

$$\xi = x/L. \quad (3.20)$$

A pressure-recovery coefficient is defined by

$$r = (p_L - p_0) / \left( \frac{1}{2} \rho \bar{u}^2 \right) \quad (3.21)$$

and a friction-factor coefficient  $K$  is defined by

$$f = K/Re \quad (3.22)$$

where  $Re$  is Reynolds number

$$Re = \frac{UD}{\nu}, \quad (3.23)$$

and  $\nu$  is the kinematic viscosity. Equation (3.19) can thus be written

$$r = 2 F_{s,0} - \frac{L}{D} \frac{1}{Re_0} \int_0^1 K [1-\xi] d\xi \quad (3.24)$$

Finally an average value of friction factor coefficient  $K$  can be defined by

$$\bar{K} = 2 \int_0^1 K [1-\xi] d\xi \quad (3.25)$$

Equation (3.24) can then be written

$$r = 2 F_{s,0} - \frac{L}{2D} \frac{\bar{K}}{Re_0} \quad (3.26)$$

Inlet Reynolds number  $Re_0$  and radial Reynolds number

$$Re_r = \frac{\bar{u}_w D}{\nu} \quad (3.27)$$

may be used interchangeably, because

$$\bar{u}_0 A_c = \bar{u}_w CL = 4 \bar{u}_w A_c L/D \quad (3.28)$$

$$Re_0 = 4(L/D) Re_r \quad (3.29)$$

Hence, Eq. (3.26) can be written

$$r = 2 F_{s,0} - \frac{K}{8 Re_r} \quad (3.30)$$

or

$$\bar{K} = 8 Re_r [2 F_{s,0} - r] \quad (3.31)$$

It is clear that, given a value of pressure recovery coefficient  $r$  from the literature, as a function of  $Re_r$  or  $Re_o$  alone for a complete condenser, and given the inlet velocity distribution so that Eq. (3.13) can be used to fix  $F_{s,0}$ , Eq. (3.31) can be used to find the average friction factor coefficient  $\bar{K}$ . It is suggested that  $\bar{K}$  be used in approximate local pressure-distribution calculations merely by employing it in Eq. (3.16) in place of the true  $K$ , as follows:

$$\frac{d\bar{p}}{dz} = - F_{s,0} \frac{d}{dz} (\rho \bar{u}^2) - \frac{\bar{K}}{Re} \frac{\rho \bar{u}^2}{2D} \quad (3.32)$$

A constant value of  $F_s$  is also used for simplicity, which is taken as the value for fully developed channel flow. While only an approximation, Eq. (3.32) will integrate to yield the correct result for  $p_L$ , since that result is built in. It is recommended that calculations be made with the approximate Eq. (3.32) and compared to more exact numerical or experimental results.

Gupta and Levy<sup>(14)</sup> report experimental results obtained with silicone oil flowing between a solid outer cylinder and a porous inner one. Results were obtained for an inner to outer radius ratio of 0.83. Due, presumably, to flow separation and turbulence,  $r$  achieved a value of only + 0.5 as radial Reynolds number  $Re_r$  becomes large. The form of Eq. (3.30) and the behavior displayed in Figures 10 and 11 of Ref. (14), suggested fitting the results with the following form of equation

$$r = A - \frac{B}{Re_r} \exp \{-[a Re_r + b Re_r^2]\} \quad (3.33)$$

In the limit of large  $Re_r$  this relation goes to the constant A (equal to 0.5 from the experimental results). At small values of  $Re_r$ ,  $r$  goes to  $-B/Re_r$  so that Eq. (3.31) gives  $K = 8B$ ; hence B must be the ordinary Poiseuille value of K divided by 8:  $B=12$  for parallel plates and 8 for the circular tube. The constants  $a$  and  $b$  govern the rapidity with which the relation goes from the  $-B/Re_r$  asymptote to the constant A asymptote. Gupta and Levy<sup>(14)</sup> also report calculated values for parallel plates.

Table 3.1 shows their values and the fit according to Eq. (3.33). The fit is within the error in reading the curve in Ref. (14). Table 3.1 also shows the values of  $\bar{K}$  corresponding to the values of  $r$  according to Eq. (3.31). The values show that, due to the fact  $2F_{s,0}$  is considerably larger than A, K increases strongly with increasing  $Re_r$ .

### 3.1.3 Flow in the Evaporating Section

In the evaporating section of a heat pipe the continual addition of mass flow requires an acceleration of the main flow which is brought about by a negative pressure gradient in the direction of flow. Viscous drag by the wall increases the magnitude of the pressure gradient. At very high rates of evaporation this factor becomes unimportant, as the velocity gradient at the wall tends to zero. At low rates of evaporation the viscous drag governs.

The analysis proceeds in the same manner as in the case of condensing regions to the approximate governing equation

$$\frac{dp}{dz} = -F_{S,L} \frac{d}{dz} (\rho \bar{u}^2) - \frac{\bar{K}}{Re} \frac{\rho \bar{u}^2}{2D} \quad (3.34)$$

Where  $F_{S,L}$  is the value of  $F_S$  at the exit of the evaporator and  $\bar{K}$  is given by

$$K = 2 \int_0^1 K_\xi d\xi \quad (3.35)$$

In this case, the subscript ( )<sub>0</sub> refers to the closed end of the evaporator and ( )<sub>L</sub> refers to the exit. The overall pressure drop coefficient defined by

TABLE 3.1  
Pressure Recovery Coefficient  
Versus Radial Reynolds Number  
For Flat Plates

Radial Reynolds Number $Re_r$	Recovery Coefficient $r$		Average Friction Factor Coefficient
	Gupta & Levy [14]	Eq. (3.33)**	$\bar{K}$ (Eq. 3.31)*
0	N.A.	$-12/Re_r$	96
1	N.A.	-9.9	98
2	N.A.	-3.9	100
3	N.A.	-1.92	104
4	-0.9	-0.97	108
5	-0.4	-0.43	113
6	-0.1	-0.09	119
7	0.1	0.13	127
8	0.3	0.28	136
10	0.5	0.45	156
12	N.A.	0.53	179
14	N.A.	0.57	205
16	N.A.	0.59	232
$\infty$		0.60	$14.4 Re_r$

\*  $F_{S,0} = 6/5$

\*\*  $A = 0.6$ ,  $B = 12$ ,  $a = 0.13$ ,  $b = 0.008$

$$r = (p_o - p_L) / \frac{1}{2} \rho \bar{u}_L \quad (3.36)$$

is related to  $K$  and  $F_{S,L}$  by

$$\bar{K} = 8 \text{Re}_r [r - 2 F_{S,L}] \quad (3.37)$$

We again fit Gupta and Levy's<sup>(14)</sup> results this time with the equation

$$r = A + \frac{B}{\text{Re}_r} \exp \{- [a \text{Re}_r + 6 \text{Re}_r^2]\} \quad (3.38)$$

As in the case of the condensing region,  $B$  is taken as the Pouiseuille value of the friction-factor coefficient (96 for flat plates) divided by 8 in order to recover Pouiseuille flow in the limit of small  $\text{Re}_r$ . Unlike the condensing region, however, in the evaporator at large values of  $\text{Re}_r$  the viscous term should vanish, thus we take

$$A = 2 F_{S,L} \quad (3.39)$$

Table 3.2 shows values of  $r$  from Ref. (14), the fit of Eq. (3.38), and  $\bar{K}$  according to Eq. (3.37).

### 3.2 EXPERIMENTAL VERIFICATION OF THE VAPOR-FLOW MODEL

In order to verify the theoretical model of vapor flow that is incorporated in GRADE II, a task was undertaken to experimentally measure the vapor pressure profile in a heat pipe that closely resembles ones typical of a spacecraft application. Figure 3.2 depicts the cross section of the experimental heat pipe. It is 188cm (74 in.) long with 19 pressure taps spaced 10.16 cm (4 in.) apart starting one inch from the evaporator end.

The pressure taps present a unique design challenge. The usual practice in measuring the static pressure of a gas stream at a wall is to drill a small-diameter hole on the order of 0.025 cm (0.010 in.) in the wall, which is connected to a pressure transducer by means of tubing. Such a small hole in a heat-pipe wall, however, would fill with liquid and the resulting capillary pressure would influence the measurement.

TABLE 3.2  
Pressure Drop Coefficient and  
Average Friction Factor Coefficient  
Versus Radial Reynolds Number

Radial Reynolds Number	Pressure Drop Coefficient		Average Friction Factor Coefficient**
	Gupta & Levy [14]	Eq. (3.38)*	
0		$12/Re_r$	96
2	8	8.21	78.6
3	6.4	6.26	71.1
4	5.5	5.31	64.4
5	4.9	4.76	58.2
6	4.4	4.40	52.7
7	4.1	4.15	47.7
8	3.9	3.97	43.1
10	3.7	3.74	35.3
12	3.6	3.60	28.9
14	3.5	3.51	23.7
16	3.4	3.45	19.4

\*  $A = 3.3$ ,  $B = 12$ ,  $a = 0.10$ ,  $b = 0$

\*\* Based upon  $F_{S,L} = A/2 = 1.65$

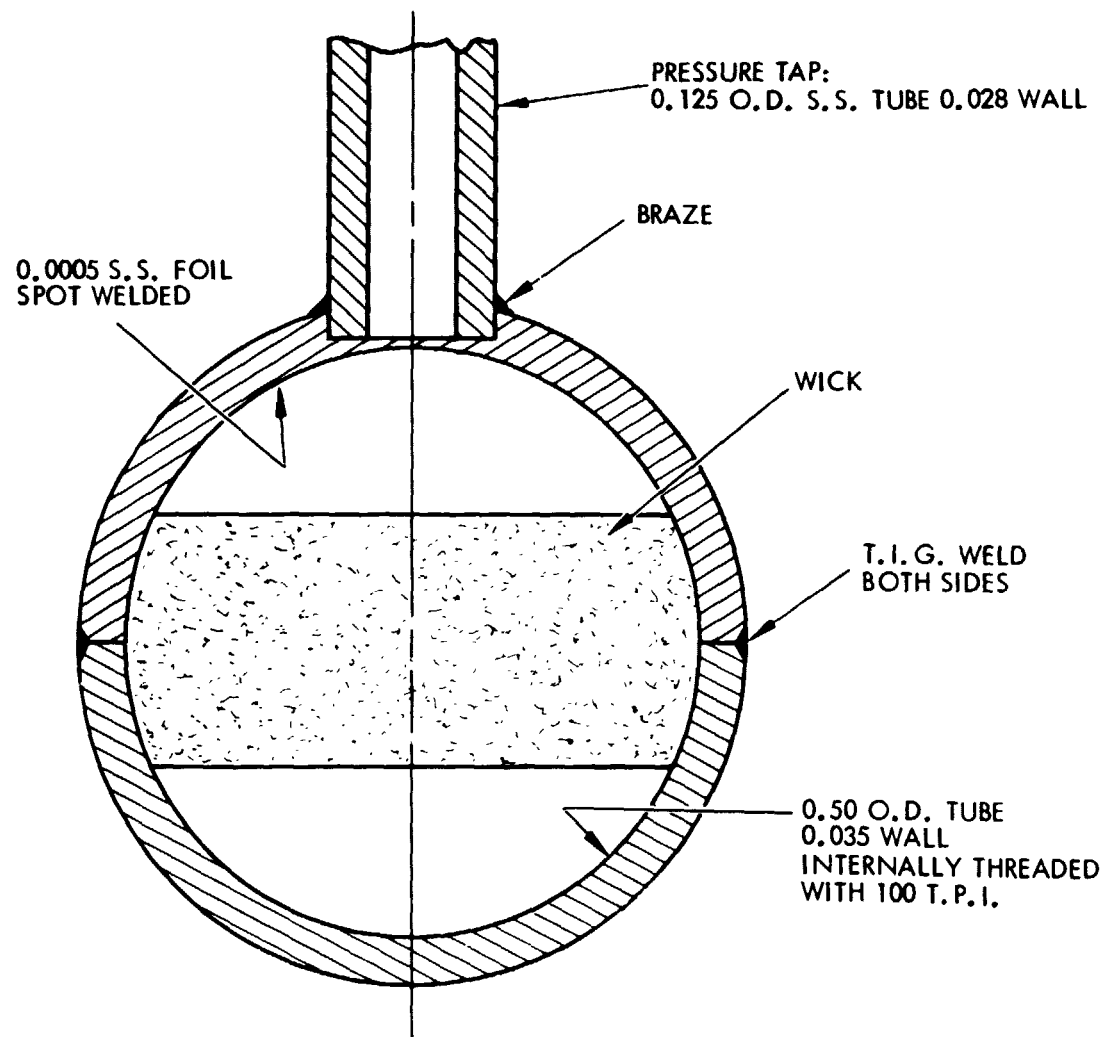


Figure 3.2 Cross Section Through Pressure Tap of Experimental Heat Pipe for Measuring Vapor-Pressure Profile



As shown in Fig. 3.2, our solution to the problem is to use a large-diameter pressure tap whose capillary pressure is insufficient to support a liquid slug. The mathematical criterion in terms of the surface tension  $\sigma$ , liquid density  $\rho$ , pressure tap I.D.,  $d$ , and heat pipe I.D.,  $D$ , is

$$4\sigma/d < \rho g D.$$

(We have assumed that the heat pipe is not overfilled, that is, there is no puddle along the bottom.) The wall hole is covered on the inside by a patch of 0.00127 cm (0.0005 in.) foil with an 0.010 inch diameter hole in it. The hole stays clear of liquid by menisci coalescence, which is the same mechanism on which the priming foil is based. A sample pressure tap was fabricated and tested. A liquid slug intentionally introduced into the tube was observed to drain away and the foil hole cleared itself by menisci coalescence.

The pressures at each tap were measured relative to the first pressure tap at the evaporator end with a Validyne variable-reluctance differential pressure transducer (0.1 psid full scale). One side of the transducer was connected to the evaporator-end tap, and the other side was connected to each of the other taps via a valve. A differential pressure measurement is made to a particular pressure tap with only the valve to that tap open.

The experimental results and the corresponding theoretical calculations by GRADE II are displayed in Fig. 3.3. Methanol is used as the working fluid since its low vapor density at room temperature results in a high vapor velocity and hence a relatively high pressure drop. Figure 3.3 shows good agreement between theory and experiment at a 20 watt heat-transfer rate and 10°C vapor temperature. The radial Reynolds number of 0.256 in the condenser section and 0.235 in the evaporator section shows that the flow is dominated by viscous effects. To increase the inertial effect, the heat transfer rate was increased and the vapor temperature was decreased. The results for 30 watts and 10°C shown in Fig. 3.3 was the highest radial Reynolds number that was obtained before the pressure readings in the condenser section became unstable and large fluctuations occurred.

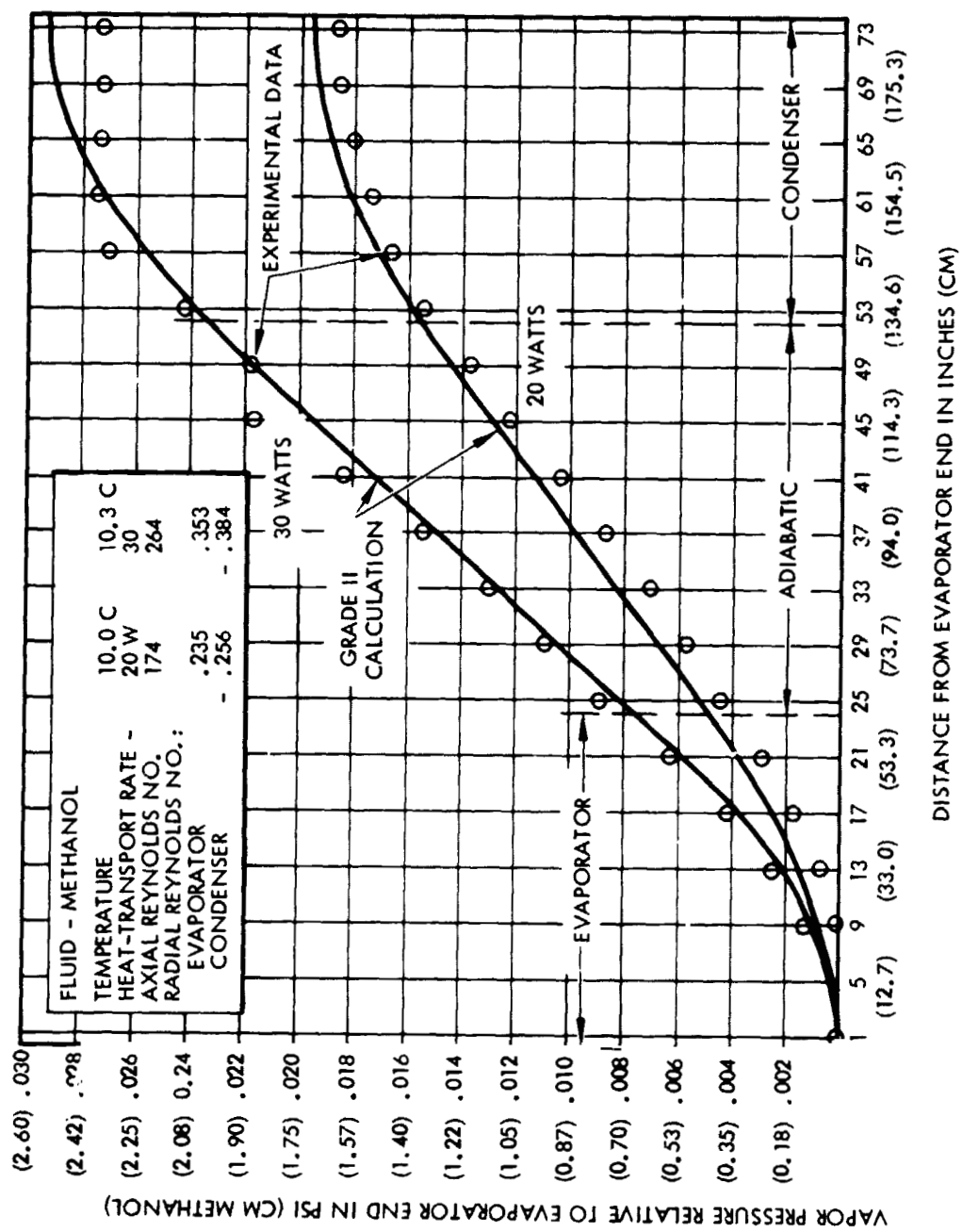


Figure 3.3 Experimental and Theoretical Vapor Pressure Profile at 20 and 30W

Instability of the flow field in the condenser region has been measured previously<sup>(13,14)</sup>, but at higher radial Reynolds numbers. We cannot completely account for the instability at such low Reynolds numbers. One factor that could strongly contribute, however, is the fact that the vapor-space surface is very rough, especially the slab wick surface. Such roughness would be expected to induce unsteady flow at a much lower Reynolds number.

## 4.0 REFERENCES

1. Edwards, D. K., Eninger, J. E., Marcus, B. D., "User's Manual for the TRW MULTIWICK Program," TRW Report 20509-6027-RU-00, prepared under NASA Contract NAS-11476, 1974.
2. For a description of FILLET and an example of its use, see "User's Manual for GRADE II," Ref (4).
3. Johnson, G. D., and Saaski, E. W., "Arterial Wick Heat Pipes," ASME publication 72-WA/HT-36, 1972.
4. Eninger, J. E., "User's Manual for GRADE II," NASA CR 137954, 1976.
5. Geir, K. D., and Edwards, D. K., "Flooding and Dry-up Limits of Circumferential Heat-Pipe Grooves," AIAA Paper No. 74-722, 1974.
6. Hsu, Wan-Chuan Joeseeph, "A Numerical Analysis of Capillary Flow in Trapezoidal Grooves during Evaporation and Condensation," Master of Science Thesis submitted to the Energy and Kinetics Dept., University of California at Los Angeles, 1976.
7. Bankston, C. A. and Smith, H. J., "Incompressible Laminar Vapor Flow in Cylindrical Heat Pipes", ASME Paper 71-WA/HT-15, 1971.
8. Tien, C. L. and Rohani, A. R., "Analysis of the Effects of Vapor Pressure Drop on Heat Pipe Performance," Int. J. Heat Mass Transfer, Vol. 17, pp. 61-27, 1974.
9. Busse, C. A., "Pressure Drop in the Vapor Phase of Long Heat Pipes," presented at the 1967 Thermionic Conversion Conference, Palo Alto, California, October 30-November 1, 1967.
10. Galowin, L. S. and Barker, V. A., "Heat Pipe Channel Flow Distributions," ASME publication 69-HT-22, 1969.
11. Galowin, L. S., Fletcher, L. W. and De Santis, M. J., "Investigation of Laminar Flow in a Porous Pipe with Variable Wall Suction," AIAA Paper No. 73-725, 1973.
12. Quaile, J. P. and Levy, E. K., "Pressure Variations in an Incompressible Laminar Tube Flow with Uniform Suction," AIAA Paper No. 72-257, 1972.